

# Topographic Effects on Internal Waves at Barkley Canyon

Kurtis Anstey

V00939802

Department of Physics and Astronomy

University of Victoria

January 10, 2022

Dr. Jody Klymak (University of Victoria)

Dr. Steven Mihaly (Ocean Networks Canada)

Dr. Richard Thomson (Institute of Ocean Sciences)

## Table of Contents

<b>List of Figures</b>	<b>4</b>
<b>1 Abstract</b>	<b>5</b>
<b>2 Introduction</b>	<b>6</b>
<b>3 Theory</b>	<b>9</b>
<b>4 Data</b>	<b>13</b>
<b>5 Methods</b>	<b>19</b>
<b>6 Results</b>	<b>25</b>
6.1 Observations . . . . .	25
6.1.1 Mean currents . . . . .	25
6.1.2 High frequency currents . . . . .	28
6.1.3 Depth dependence . . . . .	30
6.2 Frequency-dependent response . . . . .	33
6.2.1 Sub-diurnal . . . . .	33
6.2.2 Diurnal . . . . .	33
6.2.3 Near-inertial . . . . .	34
6.2.4 Semidiurnal . . . . .	40
6.2.5 Continuum . . . . .	40
6.2.6 Shoulder (incomplete) . . . . .	45
<b>7 Discussion</b>	<b>47</b>
7.1 Axis mean currents . . . . .	47
7.2 Tidal forcing . . . . .	49
7.3 Near-inertial forcing . . . . .	53
7.4 Dissipation forcing (incomplete) . . . . .	55
7.5 Spectral shoulder (incomplete) . . . . .	55
<b>8 Summary and conclusions</b>	<b>58</b>
8.1 ETC - does this writing belong anywhere? . . . . .	60
<b>9 Appendix A: Supplemental plots</b>	<b>63</b>
9.1 Wind comparisons . . . . .	63
<b>10 References (incomplete)</b>	<b>66</b>

## List of Figures

1	IW processes . . . . .	7
2	IW in a two-layer system . . . . .	8
3	IW and topography . . . . .	9
4	Barkley Canyon site map and semidiurnal criticality . . . . .	10
5	ADCP frequency, instrument ID, deployment, and data availability	11
6	Site topography . . . . .	12
7	QA threshold profiles . . . . .	13
8	Averaged stratification and WKB scaling factor . . . . .	14
9	Low-pass velocities . . . . .	15
10	Axis along-canyon mean-flow . . . . .	16
11	High-pass velocities - April 2013 . . . . .	17
12	PSD and rotary spectra . . . . .	18
13	Depth-frequency - Slope . . . . .	20
14	Depth-frequency - Axis . . . . .	21
15	Depth-band spectra - Sub-diurnal - Slope . . . . .	23
16	Depth-band spectra - Sub-diurnal - Axis . . . . .	24
17	Depth-band spectra - Diurnal - Slope . . . . .	26
18	Depth-band spectra - Diurnal - Axis . . . . .	27
19	Diurnal spring-neap forcing . . . . .	29
20	Depth-band spectra - Near-inertial - Slope . . . . .	31
21	Depth-band spectra - Near-inertial - Axis . . . . .	32
22	NI energy transfer . . . . .	34
23	NI delay histogram . . . . .	35
24	NI slab response - 2013 . . . . .	36
25	NI vertical modes . . . . .	37
26	Depth-band spectra - Semidiurnal - Slope . . . . .	38
27	Depth-band spectra - Semidiurnal - Axis . . . . .	39
28	Semidiurnal spring-neap forcing . . . . .	41
29	Depth-band spectra - Continuum - Slope . . . . .	43
30	Depth-band spectra - Continuum - Axis . . . . .	44
31	Continuum power law fits . . . . .	46
32	Continuum / GM energy ratios . . . . .	48
33	Dissipation and diffusivity . . . . .	50
34	Dissipation power law fits . . . . .	52
35	Dissipation multi-variate power law fits . . . . .	54
36	Depth-band spectra - Shoulder - Slope . . . . .	56
37	Depth-band spectra - Shoulder - Axis . . . . .	57
38	Dissipation and spectral shoulder power law . . . . .	59
39	High-frequency resolution PSD - 2013 . . . . .	60

40	Appendix A - NI wind comparisons - 2014 . . . . .	63
41	Appendix A - NI wind comparisons - 2017 . . . . .	64
42	Appendix A - NI wind comparisons - 2018 . . . . .	65

## 1 Abstract

We make use of four overlapping years of ADCP horizontal velocity time-series data near Barkley Canyon, from both slope and canyon sites, to examine the state of the local currents and internal wave field near variable topography. Results indicate expected near-shelf seasonal mean currents at the slope, and in the canyon consistent up-canyon mean currents above a near-bottom down-canyon layer. There is frequency dependent focusing of spectral power near topography, up to  $1.5 \times$  orders of magnitude 130 m above the continental slope, and up to  $2 \times$  orders of magnitude 230 m above the canyon bottom, with unique seasonality for individual constituents. There is little inter-annual variability outside of intermittent sub-diurnal and near-inertial seasonality. Sub-diurnal ( $\text{Sub}_{K1}$ ) and diurnal flows are sub-inertially trapped along topography, and the diurnal band appears to be forced locally (barotropically). The near-inertial (NI) band is attenuated near the slope, yet enhanced near the canyon bottom, with intermittent forcing that appears linked to regional wind events, high-mode propagation, and the seasonal mixed-layer depth. Free semidiurnal ( $M_2$ ) internal tides are focused and reflected near critical topography, and appear to experience both local and remote (baroclinic) forcing. A near-topography enhanced internal wave continuum (up to  $7 \times$  GM) indicates increased rates of dissipation ( $\epsilon$ , exceeding  $10^{-8}$  W/kg) and diffusivity (exceeding  $10^{-4}$  m<sup>2</sup>/s). Power-dissipation seasonality correlations suggest a cascade of energy from the semidiurnal constituent, yielding inter-annual power law relationships of  $\epsilon \sim M_2^{0.42}$  at the slope, and  $\epsilon \sim M_2^{0.64}$  in the canyon. Improved fits accounting for secondary constituents ( $\text{Sub}_{K1}$  on the slope, and NI in the canyon yield) yield power law relationships of  $\epsilon \sim M_2^{0.83} + \text{Sub}_{K1}^{0.59}$  at the slope, and  $\epsilon \sim M_2^{1.47} + \text{NI}^{0.24}$  in the canyon. There is also evidence of a spectral shoulder near  $N$  which shares power seasonality with the internal wave continuum, yielding a power law relationship of  $P_{sh} \sim \epsilon^{0.36}$  at the slope, and  $P_{sh} \sim \epsilon^{0.48}$  in the canyon.

## 2 Introduction

Internal waves (IW) are slow-moving, low-frequency, sub-surface gravity waves that exist within density gradients in the ocean interior (Garrett & Munk, 1979). They have wavelengths up to kilometres long, and oscillate in a range between the local Coriolis (inertial,  $f$ ) and Brunt–Väisälä (buoyancy,  $N$ ) frequencies (Garrett & Munk, 1979). They are forced by weather - as near-inertial (NI) IW are generated by surface winds exciting currents in the mixed layer that 'pump' energy into the IW field, below (Garratt, 1977) - or by tides and currents moving over irregular seafloor topography, generating baroclinic waves that can propagate through the stratified ocean (Hendershott & Garrett, 2018). Nonlinear interactions with irregular topography can cause incident IW to scatter, reflect, or focus and break, leading to mixing (Martini et al., 2013).

As the wind, currents, and tides are ever-present, IW are prevalent ocean phenomena. As early as the mid-19th century, scientists such as Stokes and Rayleigh were investigating properties of fluid density and stratification, essential for IW propagation (Garrett & Munk, 1979). IW were mistaken as consistent noise in early 20th-century hydrocast readings, and Ekman discussed their effects in his seminal theories on fluid mechanics (Garrett & Munk, 1979). In the late-20th century, Garrett and Munk (1979) developed the canonical Garrett-Munk (GM) spectrum defining the characteristic frequency and wavenumber continuum of open-ocean IW, to better understand their role in ocean processes. As instrumentation improved, scientists continued to uncover the contributions of IW to physical systems of all scales, such as fine-scale mixing or the large-scale overturning circulation (Figure 1; Garrett & Munk, 1979). Recent studies have focused on IW generation and dissipation (Terker et al., 2014; Kunze, 2017), tidal and wind forcing and seasonal variability (Alford et al., 2012; Thomson & Krassovski, 2015), and enhanced mixing due to IW interactions with irregular topography (Nash et al., 2004; Kunze et al., 2012; Gemmrich & Klymak, 2015).

As IW and internal tides (IT) approach seamounts, slopes, or canyons, their energy is focused and can cascade from low- to high-frequency processes, eventually dissipating as heat (Garrett & Munk, 1979; Klymak, 2006). Dissipation leads to an energetic local environment, evident as turbulent processes on the fine- (1 - 100 m vertical) and micro-scales ( $< 1$  m vertical) (Garrett & Munk, 1979; Kunze et al., 2012). These processes cause the mixing of heat, pollutants, and biological constituents, and drive regional transport of energy and momentum (Kunze et al., 2012). Topography-forced IW mixing helps set ocean stratification, layers that influence both small- and large-scale physical systems (Garrett & Munk, 1979). As such, knowledge of topography-IW

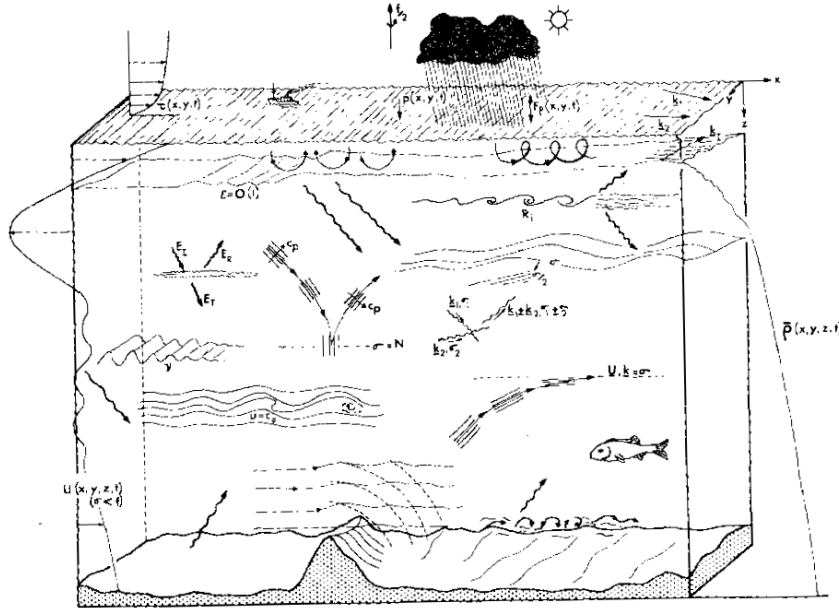


**Figure 1.** Generalised depiction of IW processes in the ocean, as envisioned by Garrett and Munk (1979). IW are forced by, coincide with, or contribute to most physical processes in the ocean.

interactions is important for understanding both regional dynamics and the large-scale ocean-atmosphere coupled climate system (Garett & Munk, 1979).

Topography focused IW studies are global, ongoing at locations such as the Hawaiian ridge (Alford et al., 2007), the continental slopes of the South China Sea (Klymak et al., 2011), and the slope-incising submarine canyons of the northeast Pacific (Allen et al., 2001; Carter & Gregg, 2002; Kunze et al., 2012; Terker et al., 2014). Canyons and their adjacent continental slopes have been identified as hot spots of IW activity, that both generate (Carter & Gregg, 2002) and dissipate (Allen et al., 2001; Kunze et al., 2002) IW and IT. At Monterey Canyon, IW and IT have been found to scatter, reflect, and focus depending on the relative angle of incident IW and the impacted topography (Figure 3; Kunze et al., 2012); force near-bottom turbulent layers that drive mixing (Carter & Gregg, 2002; Kunze et al., 2002); and, cause dissipation and IT generation near irregular topography (Terker et al., 2014). Further research on IW interactions with submarine canyons and their adjacent continental slopes is thought to be essential to understanding seasonal upwelling, diapycnal mixing, and cross-shelf exchange (Burrier, 2019).

In Canada, IW are regularly observed on the highly productive Vancouver Island Continental Shelf (VICS) (Allen et al., 2001), a relatively broad (about

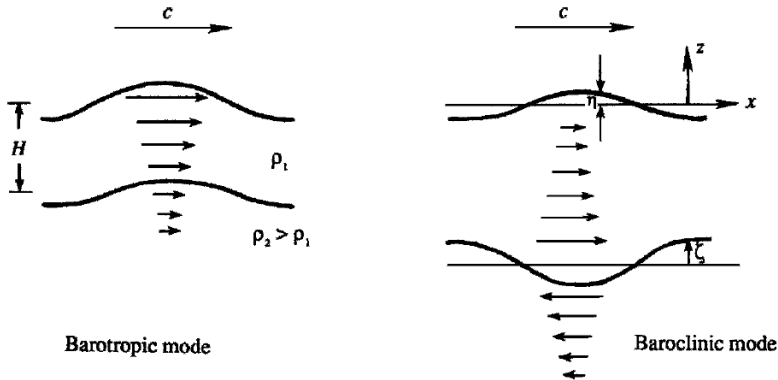


**Figure 2.** IW in a two-layer system. Graphic representation of the difference between barotropic and baroclinic flows. Adapted from Kundu & Cohen (2008).

80 km) shelf region with a canyon-incised continental slope. Regional IW observations have led to insight on non-linear wave-wave interactions between surface generated NI IW and upward propagating semidiurnal IT (Mihaly et al., 1998), and the presence of diurnal baroclinic shelf waves forced by tidal oscillations near the mouth of the Juan de Fuca Strait (Thomson & Crawford, 1982). Seasonally variable regional currents (Thomsons & Krassovski, 2015) have been associated with observations of vorticity stretching and upwelling at the head of the shelf-incising Barkley Canyon, suggesting considerable canyon influence on local water properties, transport of biological constituents, and overall shelf productivity (Allen et al., 2001; Juniper et al., 2013; Doya et al., 2013; Chauvet et al., 2018). However, there is a lack of topography-IW observations necessary to fully understand the Barkley Canyon region's influence on the physical processes of the VICS. Further research into the IW field at Barkley Canyon can provide insight into regional mixing characteristics effects, as well as an additional case study for topography-IW research, globally.

To contribute to this effort, this study evaluates horizontal velocity data from two Barkley Canyon sites, one on the adjacent continental slope and one within the canyon, to characterise the interactions of IW and IT with topography, and the potential influence on local mixing. Mean currents are characterised, and sub-tidal, tidal, NI, and super-tidal (IW continuum and above- $N$ ) frequency bands are evaluated for depth-dependence and seasonality, including a forcing analysis of variability due to mean currents, tides, and wind. The state of the high-frequency IW continuum is evaluated for topographic enhancement through comparison with canonical GM theory, estimates of dissipation and diffusivity to estimate mixing. Key findings include topography guided current

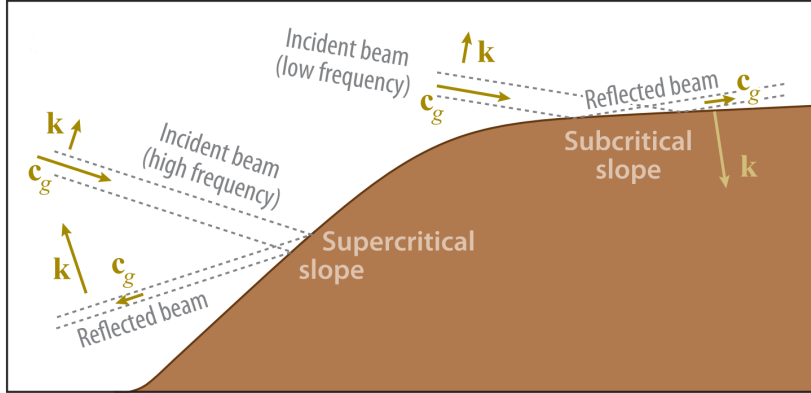


**Figure 3.** Graphic of IW interactions with slope topography (Lamb, 2014). The propagation angle of an IW depends on frequency and stratification. Depending on the slope of topography, incident IW can be scattered up, reflected down, or focused, possibly breaking.

layers, near-topography enhancement of IW spectral power with frequency-dependent seasonality, NI IW attenuation near the continental slope with intermittent forcing from wind events, and a heightened IW continuum state with power-dissipation seasonality correlations suggesting a cascade of energy from the semidiurnal frequency constituent.

### 3 Theory

Vertical displacements in a fluid can be classified as either barotropic, where the displacement is dependent only on pressure,  $P(z)$  (where  $z$  is depth), or as baroclinic, where the displacement is also a function of density,  $\rho(z)$ , temperature,  $T(z)$ , etc. (Figure 2). For example, the surface tides are barotropic, affecting most of the water column as the surface oscillates, while IW are baroclinic, perturbations that exist along density interfaces in the stratified ocean interior. IW are highly dependent on stratification, often characterised by the depth-dependent buoyancy frequency,  $N(z)$ , defined as:

$$N^2(z) = -\frac{g}{\rho_0} \frac{d\rho}{dz} \quad (1)$$

where  $g$  is the acceleration due to gravity, and  $\rho_0$  a constant reference density. In continuously stratified fluids such as the ocean interior, IW may exist both non-isotropically and rotationally, with rotation effects defined by the consistency relation

$$\frac{CW}{CCW} = \frac{(\omega + f)^2}{(\omega - f)^2} \quad (2)$$

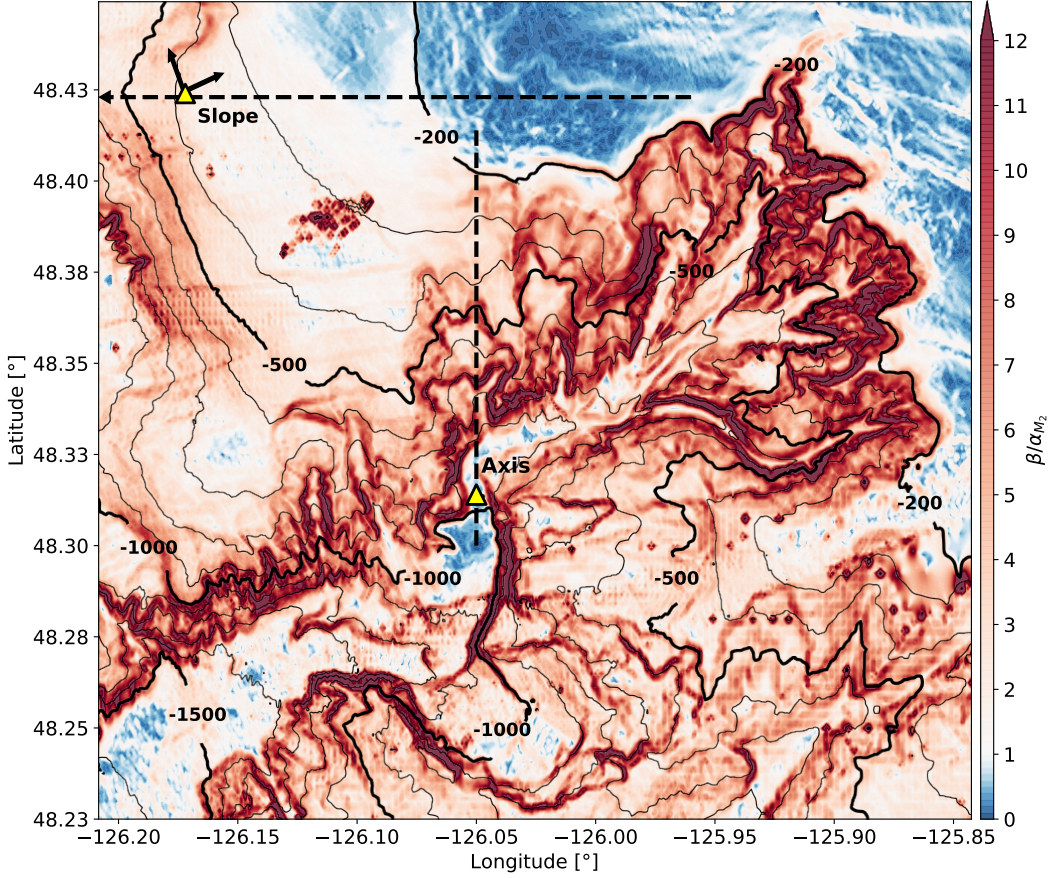


**Figure 4.** Site map and semidiurnal criticality of Barkley Canyon. Criticality is found by dividing the gradient slope ( $\beta$ ) of topography by the depth-dependent semidiurnal propagation angle ( $\alpha_{M_2}$ ). Most of the region is supercritical ( $> 1$ ) to the  $M_2$  IT, with notable exceptions on the shelf and canyon floor near the Axis site. Arrows at the Slope site indicate  $30^\circ$  rotation of velocity data to match approximate along-slope ( $v$ ) direction of mean currents; Axis data were not rotated, as the along-canyon ( $v$ ) component is aligned N-S. Dashed black lines indicate topography cross-sections used in Figure 6.

where  $\omega$  is frequency,  $f$  the Coriolis frequency ( $f = 2\Omega \sin \phi$ , where  $\Omega$  is the rotation rate of the Earth, and  $\phi$  is latitude).  $f$  and  $N(z)$  are the lower and upper frequency bounds for free IW (Kundu and Cohen, 2008). IW generated outside this frequency range are evanescent (trapped) to topography, unable to radiate into the ocean interior (Flather, 1988).

As free IW and IT approach irregular topography (continental slopes, canyons, etc.), the angle of the incident wave energy,  $\alpha$ , and the slope of the topography,  $\beta$ , have an influential relationship on the behaviour of the interaction (Figure 3) (Lamb, 2014). The ray path of an incident, free IW in a continuously

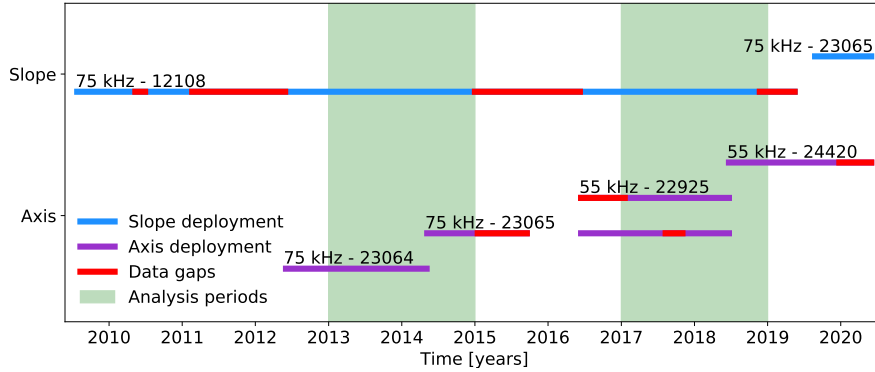


**Figure 5.** ADCP operating frequency, instrument ID, deployment periods, and data availability for the Slope and Axis sites. ONC operates and maintains regional instruments as part of the NEPTUNE cabled observatory. Due to maintenance and redeployment, years with comprehensive overlapping coverage (2013, 2014, 2017, and 2018) were selected for analysis.

stratified fluid is:

$$\alpha(z) = \sqrt{\frac{(\omega^2 - f^2)}{(N(z)^2 - \omega^2)}} \quad (3)$$

(Nash et al., 2004; Garrett and Kunze, 2007; Lamb, 2014). The impacted bathymetric slope,  $\beta = \nabla H$ , is determined from the gradient magnitude of the local topography, and used to determine regions of IW and IT criticality as, as in Figure 4 (Martini et al., 2011). As  $\alpha$  depends on  $N(z)$ , the characteristic ray path of an IW bends with depth. If  $\beta > \alpha$  a slope is supercritical and incident wave energy is reflected downward (see Figure 6); for  $\beta \approx \alpha$  a slope is near-critical and incident wave energy is focused, potentially leading to non-linear breaking and dissipation; and, for  $\beta < \alpha$  the slope is considered subcritical and incident wave energy is scattered upward (Klymak et al., 2011). The combined effects of reflection, scattering, and focusing of IW and IT in near-critical regions can lead to an energetic environment near topography (Lamb, 2014).

Regions near-critical to tidal frequencies are known as hot-spots for generation of baroclinic IT, including continental slope, shelf-break, and canyon topography, though IT can also be generated over non-critical irregular topography through the friction of tidal oscillations (Garrett and Kunze, 2007). Topographically generated IT that are within the frequency bounds of  $f$  and  $N(z)$  radiate away baroclinically, while those outside these bounds are trapped along topography (Kunze, 2012). Near-shore, at latitudes where the oscillating tidal frequency is sub-inertial, baroclinic 'shelf waves' can still be generated over

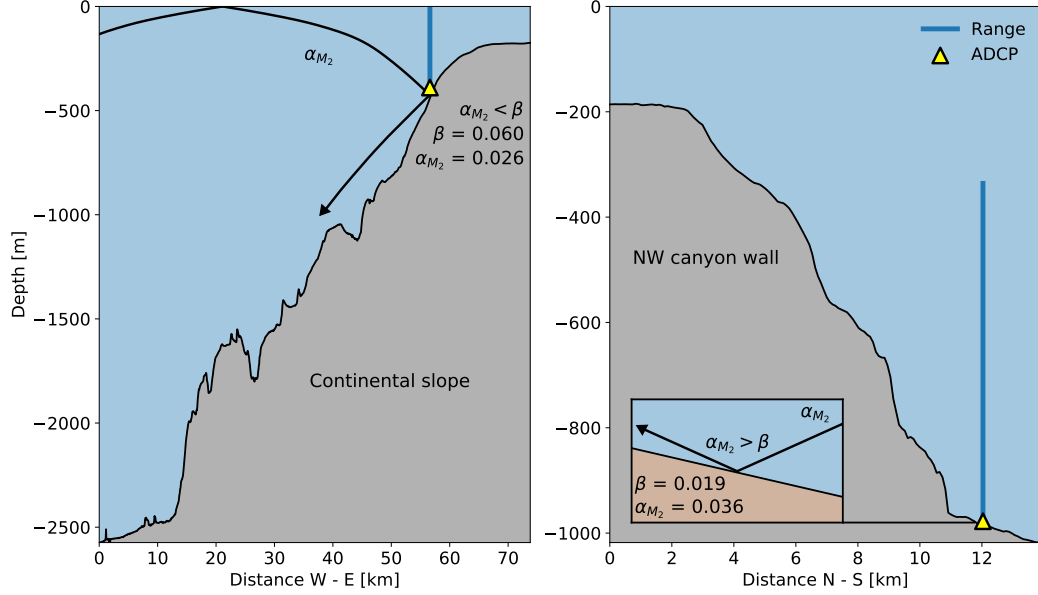


**Figure 6.** Site topography cross-sections with ray tracing. Depicted are the relative locations for Slope (left) and Axis (right) instrument moorings. Horizontal cross-sections were taken in the W-E (Slope) and N-S (Axis) directions, represented by the dashed black lines in Figure 4. Slope sits below the VICS shelf-break while Axis is located on the floor of Barkley Canyon (right). An incident ray is shown for  $M_2$ , accounting for depth-dependent stratification, as well as local criticality at each site.  $\alpha$  is the angle of propagation, and  $\beta$  is the slope of the topography. In general, the Slope region is supercritical, while the Axis region is both subcritical (floor) and supercritical (walls).

irregular topography, trapped along the continental margin where the topographic gradient of the shelf acts as a restoring force for horizontal propagation (Crawford and Thomson, 1984; Brink, 1991).

In addition to topographically generated IW and IT, there is significant input into the oceanic IW field from wind (Alford et al., 2016). NI energy is deposited into the surface mixed-layer (ML), forcing NI currents that 'strum' IW modes; the relative rotation and propagation of these modes moves energy downward to the base of the thermocline, then into the interior (Zervakis and Levine, 1995). Generated NI IW propagate downward and equatorward into the ocean interior (Alford et al., 2016). For a flat-bottom basin bounded by the ocean surface, the vertical structure of IW modes exist as solutions to the Sturm-Liouville equation (Alford and Zhao, 2007):

$$\frac{\partial^2}{\partial z^2}\eta(z) + \frac{N^2(z)}{c_n^2}\eta(z) = 0 \quad (4)$$

with boundary conditions  $\eta(0) = \eta(D) = 0$ , where  $D$  is the total water depth,  $\eta$  is surface displacement,  $n$  the mode number, and  $c_n$  the modal eigenspeed.

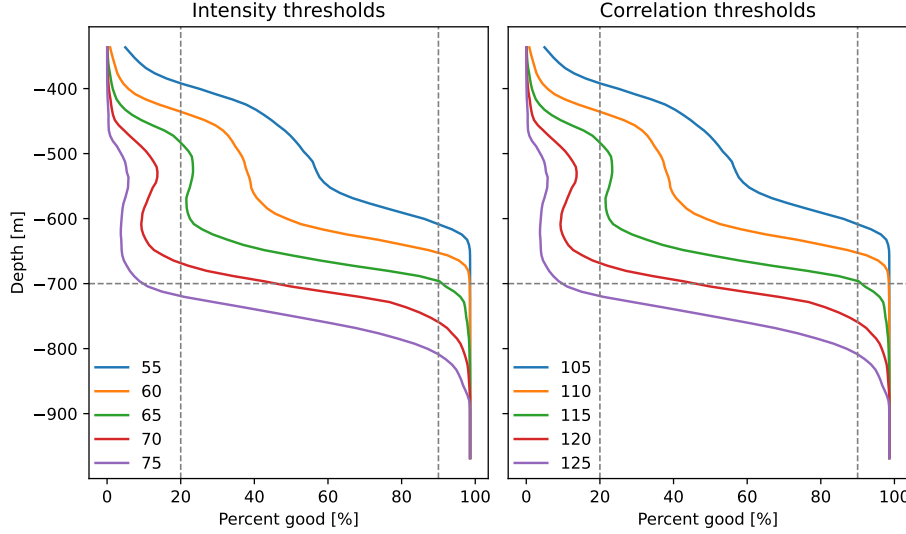


**Figure 7.** QA threshold profiles. Backscatter intensity and beam correlation percent-good vertical profiles for various thresholds. The green line in each was selected as the ideal threshold value due to the step-function-like steepness of the profile at 20 and 90%, in addition to the qualitative removal of depth-dependent processing artifacts and near-surface side-lobe contamination when used together as a screen.

Low-modes tend to dominate NI IW energy and largely propagate horizontally, while high-mode energy typically radiates downward (Alford et al., 2016). Seasonal NI mode amplitudes can be found with ML depth as a time-dependent step-function for convolution with the ML NI currents, as determined by a slab model (discussed in Section 5). In general, the superposition of many modes forms an IW beam (Lamb, 2014). The vertical propagation of IW energy is then defined by the dispersion relation (Alford, 2012, 2013):

$$c_{gz} = \frac{\omega^2 - f^2}{\omega m} \quad (5)$$

where  $m$  is the vertical wavenumber.

## 4 Data

The obtained Barkley Canyon horizontal velocity data is unique for both spatial and temporal considerations. Located at approximately 48.33°N 126.03°W, the Barkley Canyon region is about 75 km southwest of the coast of Vancouver Island, incising the continental slope and shelf (Figure 4). Barkley Canyon is a winding canyon up to 6 km wide and 13 km long, with an adjacent shelf-break region beginning around -150 m depth. Spread across the region, Acoustic

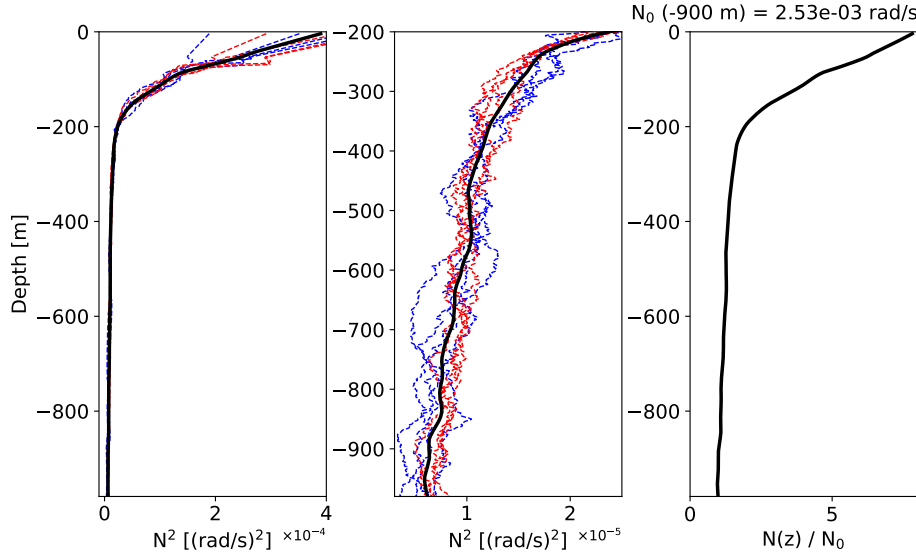


**Figure 8.**  $N^2$  parameter and WKB scaling factor. Buoyancy results were smoothed and averaged for the four analysis years at La Perouse station LB14 CTD data, and are displayed through the water column (left) and below -200 m (centre). Casts were taken in May (blue) and September (red). A WKB scaling factor (right) was determined for use in Equation 9, based on  $N_0$  averaged around -900 m.

Doppler Current Profilers (ADCP) provide current data for Ocean Networks Canada's (ONC) NEPTUNE cabled observatory. ADCP emit acoustic beams that triangulate Doppler shifts in the water column, providing directional velocity data time series through depth. The placement of ADCP across both continental slope and canyon topography allows for spatial analysis of coinciding IW events. Furthermore, ONC's Oceans 2.0 data portal offers publicly available processed data for each instrument, spanning over a decade. As such, the obtained datasets are substantially lengthy for IW research, allowing for typically difficult analysis of long-term variability.

The two ADCP for this study are located at the upper continental slope Upper Slope (Slope) and canyon-floor Axis sites (Figure 4). The Slope platform sits below the VICS shelf-break at a depth of -378 m (Figure 6), 15 km NW of Barkley Canyon, employing primarily 75 kHz ADCPs. The Axis platform is located at a narrow north-south channel on the floor of Barkley Canyon, about midway along its length at a sharp bend, and a depth of -968 m (Figure 6), employing both 75 and 55 kHz ADCPs. The 75 kHz Teledyne RDI Workhorse Long Ranger instruments were set to a vertical resolution of 8 m depth bins, and a continuous sampling rate of 2 seconds. The 55 kHz Nortek Signature55 instrument was set to a vertical resolution of 20 m depth bins, and a pulsed

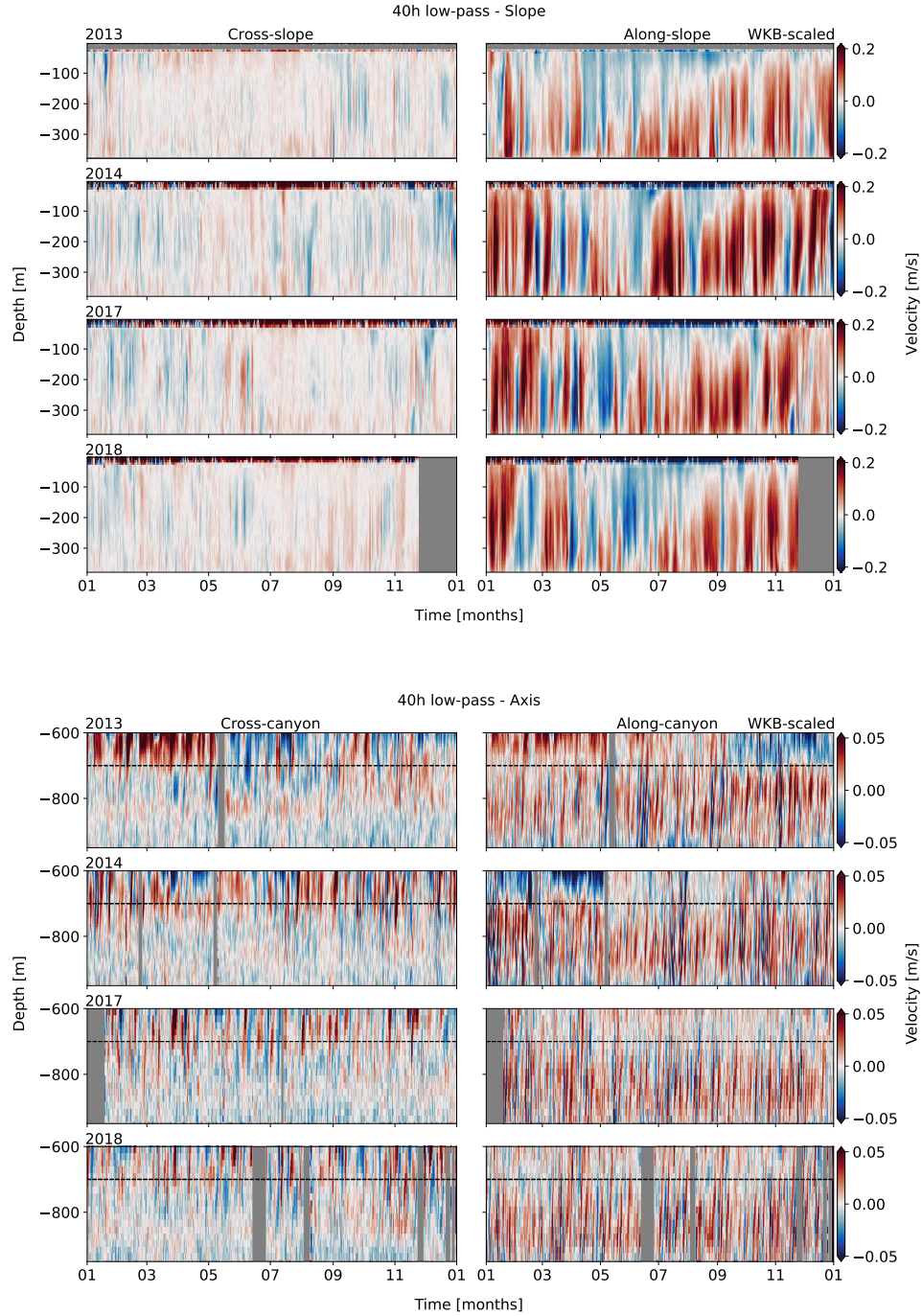


**Figure 9.** 40-hour low-pass WKB-scaled horizontal velocity data for Slope (top) and Axis (bottom). Components are separated as cross- (left) and along-slope/canyon (right). At Axis, the dashed line is the upper limit of the analysis depths (-650 m). There is a clear seasonal cycle in the along-slope component at Slope, while seasonality is less apparent in the predominantly along-canyon flow at Axis.

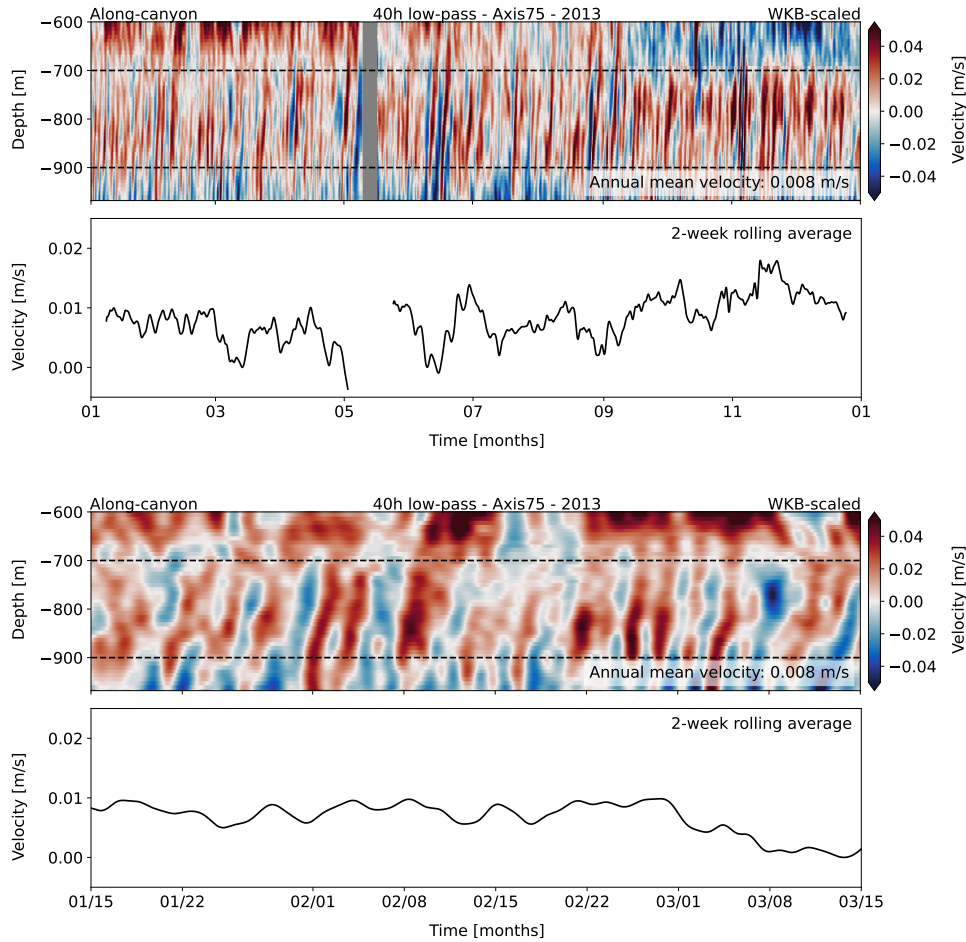


**Figure 10.** 40-hour low-pass WKB-scaled horizontal velocity data showing along-canyon mean currents for Axis, annually (top) and in a two-month snapshot (bottom). Mean up-canyon flow is within the dashed lines; a thin near-bottom layer of mean down-canyon flow is below.

sampling rate of six 18-second pings followed by a 4.5-minute delay. For these sites, overlapping data coverage of good quality (e.g. minimal data gaps) is during 2013, 2014, 2017, and 2018 (Figure 5), due to ONC deployment and maintenance schedules.

An initial quality check of backscatter intensity and beam correlation was performed for the raw data (Figure 7), yielding quality thresholds of 65 and 115 counts, respectively. There is some seasonal variation in the vertical percent-good profiles based on these thresholds, notably in the fall, likely associated with seasonality of biological scatterers higher in the water column. Time-averaged profiles indicate regions of good data ( $\geq 90\%$  good) below -50 m

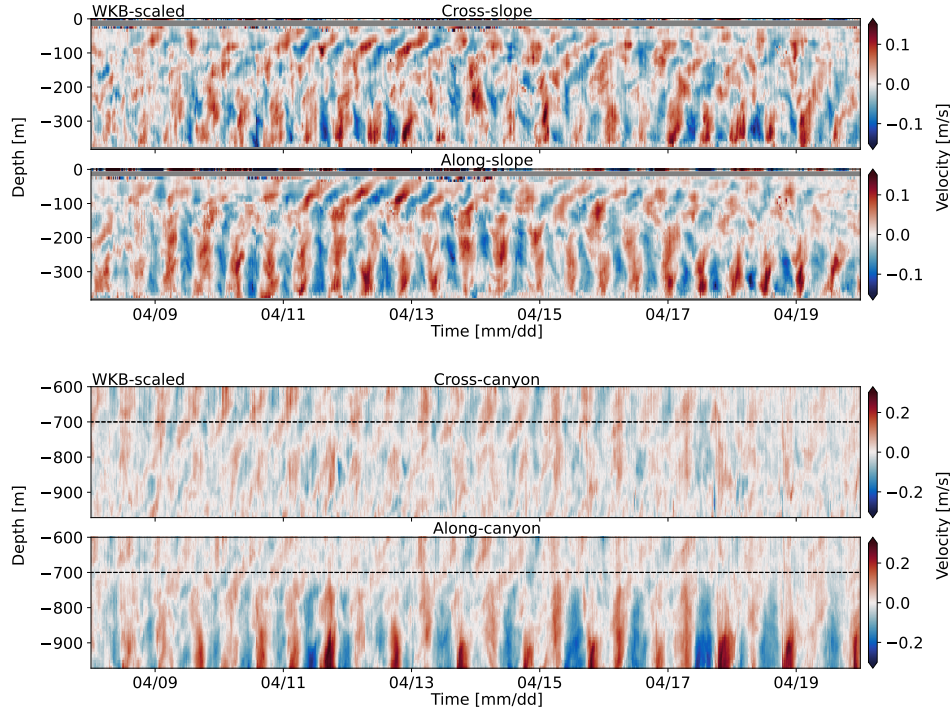


**Figure 11.** 40-hour high frequency WKB-scaled horizontal velocity data for Slope (top) and Axis (bottom), in April 2013. Components are separated as cross- (upper) and along-slope/canyon (lower). There are IW and IT of varied frequency, non-uniform vertical structure, and depth-dependence.

at Slope, and below -700 m at Axis. These depths avoids near-surface side-lobe contamination, and depth-dependent processing artifacts - non-physical high-frequency spikes in power spectra evident above about -600 m. For Axis instruments, with range well above the cut-off depth, up to -600 m is retained in plots for reference, and a line at -700 m indicates the upper extent of the analysis region.

Datasets were then acquired in 15-minute averaged sampling intervals for each analysis year, and combined and mapped to standard depth bins. Gaps were interpolated using a linear process for gaps less than 25 hours. For large data gaps, annual datasets were combined using weighted averaging as necessary. All supplemental processing materials, including Python code and plots, are available in the project GitHub repository (Anstey, 2022).

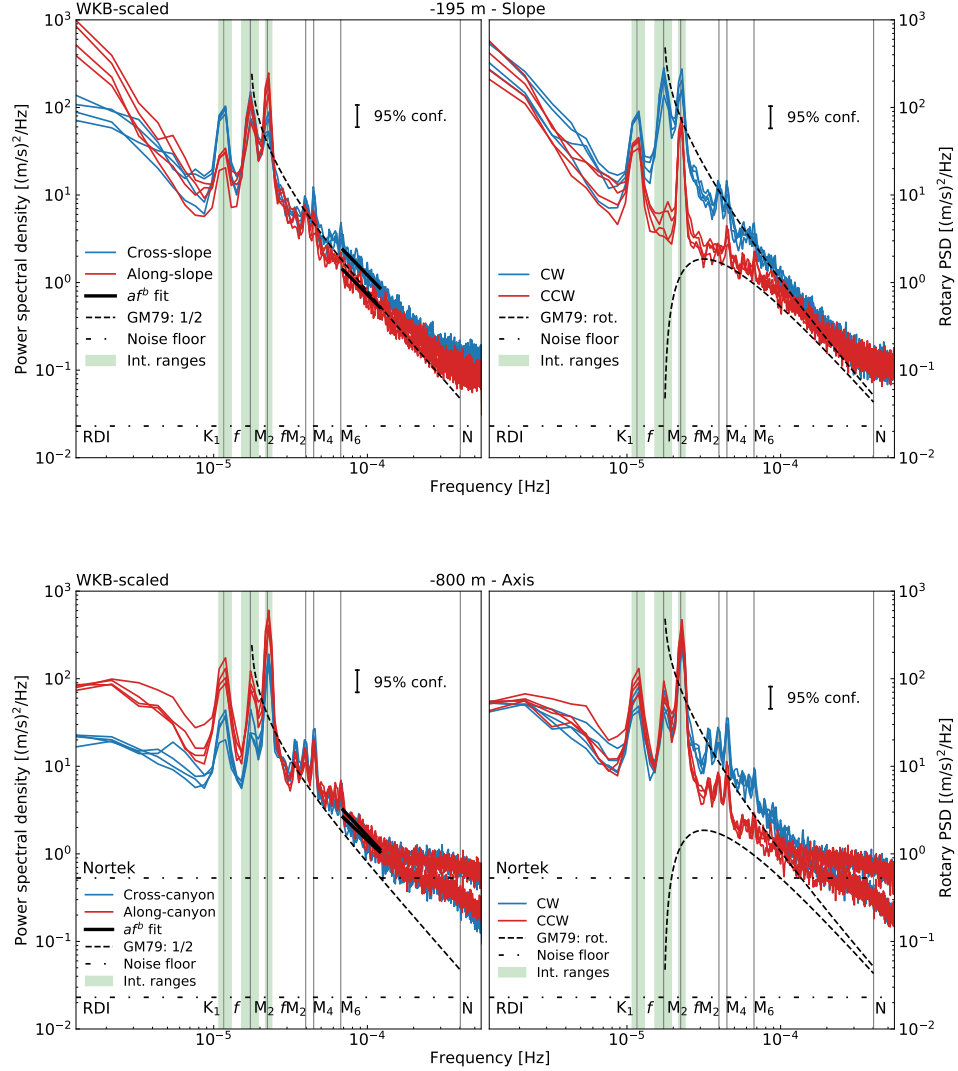


**Figure 12.** Mid-depth annual PSD (left) and rotary (right) spectra of WKB-scaled horizontal velocity data, for Slope (top) and Axis (bottom). Each line of the same colour is a different year. For PSD, cross- (blue) and along-slope/canyon (red) components are shown; for rotary, CW (blue) and CCW (red) components are shown. 95% confidence intervals are indicated by the black bar. Instrument noise floors (dotted line) and primary frequency constituents with integration range (vertical lines and green shading) are shown. For PSD, black lines indicate continuum power-law fit, and the dashed line is the GM79 spectrum (1/2 amplitude). For rotary, the GM79 spectrum is in rotary components (CW upper). Spectra at both sites are characteristically red, with prominent tidal and NI peaks.

## 5 Methods

At Slope, horizontal velocity data were rotated using a standard rotation matrix:

$$u_{rot} = u\cos(\theta) - v\sin(\theta) \quad (6)$$

$$v_{rot} = u\sin(\theta) + v\cos(\theta) \quad (7)$$

where  $\theta$  is the rotation angle in radians. This better matches the physical cross-slope angle of approximately  $30^\circ$ ;  $u$  is referred to as cross-slope, and  $v$  as along-slope (Figure 4). At Axis, the along-canyon ( $v$ ) direction is approximately north-south, so no rotation was necessary;  $u$  is 'cross-canyon'.

To account for depth-dependent stratification, horizontal velocity data were WKB-scaled as:

$$u_{WKB}(z) = u(z)\sqrt{\frac{N_0}{N(z)}} \quad (8)$$

and for energy density as:

$$\phi_{WKB}(z) = \phi(z)\frac{N_0}{N(z)} \quad (9)$$

with a reference buoyancy frequency of  $N_0 = 2.53 \times 10^{-3}$  rad/s averaged around -900 m (Althaus et al., 2003). Buoyancy data were determined from climatology data obtained from the nearby (20 km S) station LB14. Data were sampled annually in May and September, during Fisheries and Oceans Canada (DFO) La Perouse cruises, casting down to -1180 m. Depth profiles were obtained for temperature, pressure, and salinity,  $S(z)$ , to find potential density,  $\rho_\theta(z)$ , following the UNESCO 1983 (EOS 80) polynomial. Depth-dependent buoyancy was then determined as in Equation 1 (Figure 8). There is little inter-annual variability in the buoyancy depth profiles.

Component-wise power spectral density (PSD) was determined from the WKB-scaled horizontal velocity data for each depth bin, using a Welch spectrogram process with a Hanning window of 256 data-points ( $\sim 2.7$  days), 50% overlap, and detrended in time to avoid a 0 Hz offset. For comparison, additional 'fine' (short window, poor frequency-resolution) and 'coarse' (long window, greater frequency-resolution) time-resolution spectra were computed with 128 ( $\sim 1.3$  days) and 512 ( $\sim 5.3$  days) data-points per window, respectively. The noise floor of each instrument was determined from the standard error of the mean relative to instrument sampling intervals and uncertainties from Nortek and RDI. 95% confidence intervals were determined using a chi<sup>2</sup> method.

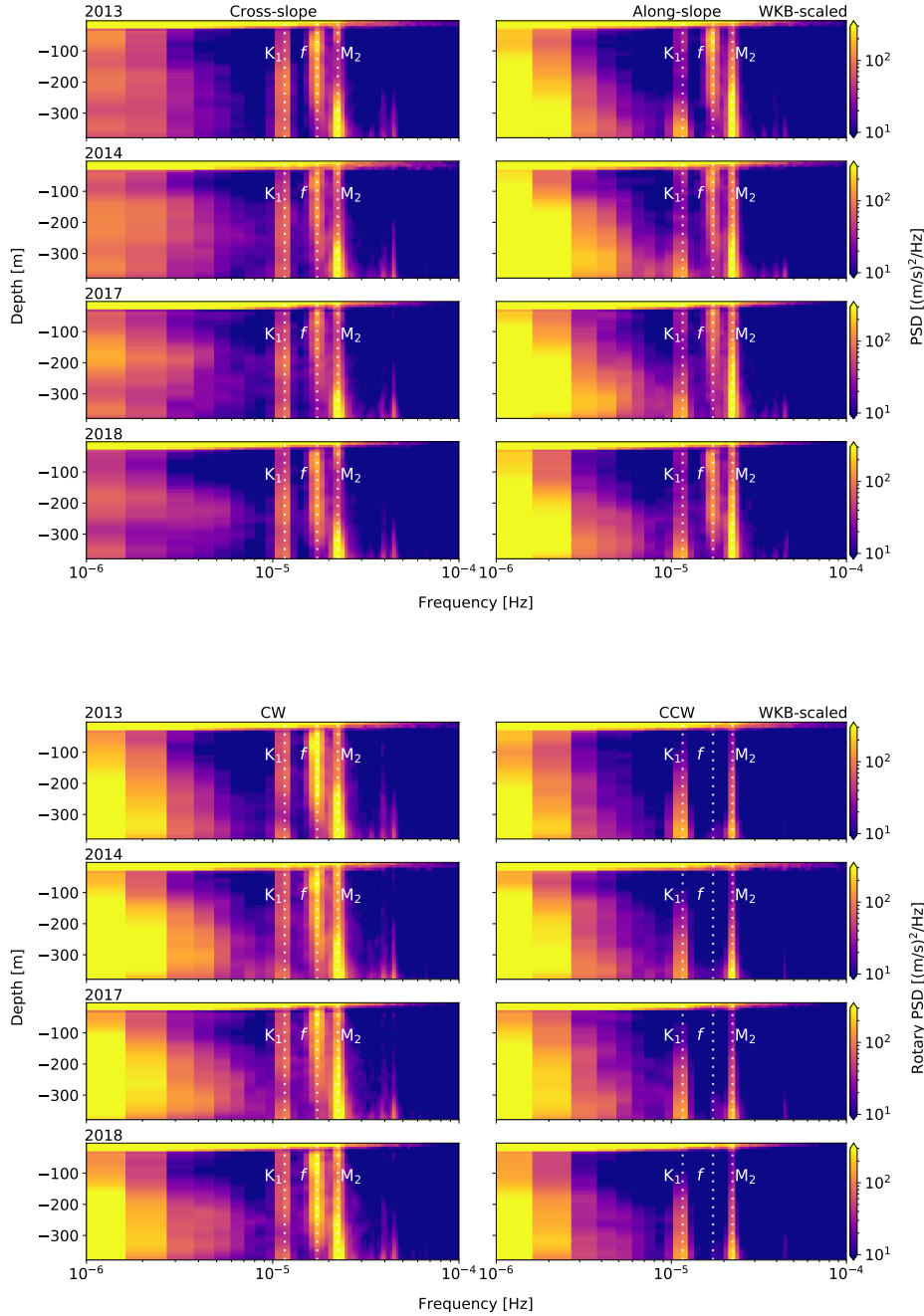


**Figure 13.** Depth-frequency PSD (top) and rotary spectra (bottom) for Slope. Components are separated as cross-/CW (left) and along-slope/CCW (right). Determined from WKB-scaled horizontal velocity data. There is near-bottom intensification of individual frequency constituents (and near-bottom attenuation of the NI band).

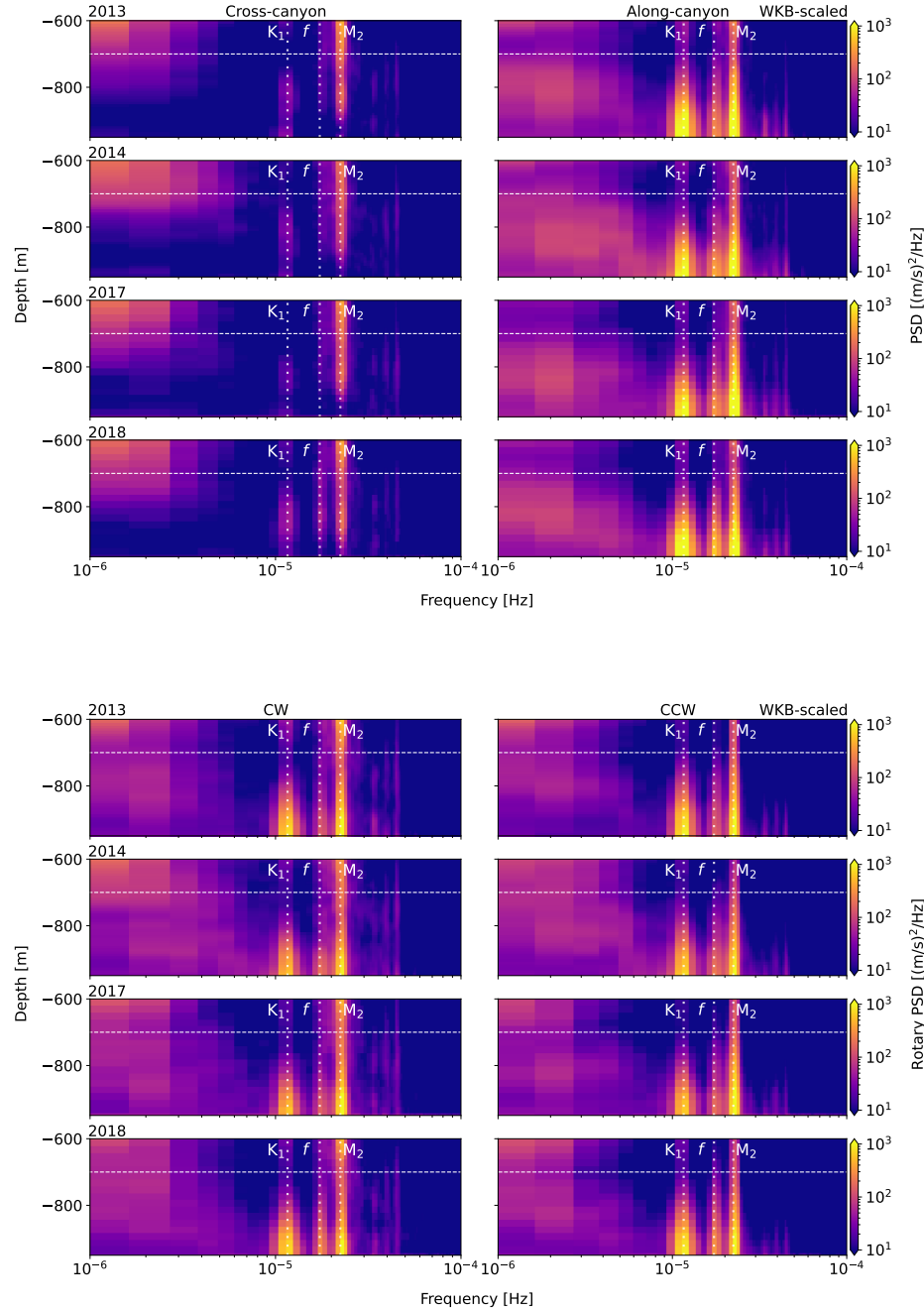


**Figure 14.** Depth-frequency PSD (top) and rotary spectra (bottom) for Axis. Components are separated as cross-/CW (left) and along-canyon/CCW (right). Determined from WKB-scaled horizontal velocity data. Dashed line indicates upper depth limit for analysis. There is near-bottom intensification of individual frequency constituents.

For rotational dependence, rotary power spectra were determined as for PSD, though using a modified spectrogram process based on the work of Gonella (1972) and Thomson and Emery (2014). To summarise, the adjustment to find the counter-clockwise (CCW) and clockwise (CW) components of a complex horizontal velocity vector,  $\mathbf{w}(t) = u(t) + iv(t)$ , is the addition or subtraction of twice its quadrature spectrum,  $Q_{uv}$ , as:

$$\text{CCW} = \frac{1}{2}[S_{uu} + S_{vv} + 2Q_{uv}] \quad (10)$$

$$\text{CW} = \frac{1}{2}[S_{uu} + S_{vv} - 2Q_{uv}] \quad (11)$$

where  $S_{uu}$  and  $S_{vv}$  are the typical complex autospectra used for PSD (Thomson & Emery, 2014). In general, a stronger CW component indicates downward propagation of energy, and vice-versa.

The open-ocean GM IW spectrum was determined following a process adapted from Callies (2016), using local parameters for  $f = 1.73 \times 10^{-5}$  Hz,  $g = 9.81(m/s)^2$ , and  $N_0$ , along with canonical values for the surface-extrapolated buoyancy frequency ( $N_{GM} = 5.24 \times 10^{-3}$  rad/s), e-folding scale of  $N(z)$  ( $1.3 \times 10^3$  m), mode scale number  $j* = 3$ , and dimensionless IW energy parameter  $E = 6.3 \times 10^{-5}$ , as in Munk and Wunsch (1981). The directional GM spectrum was adapted to rotary form through application of the rotary consistency relation, as described in Section 3 (Levine et al., 2002; Polzin & Lvov, 2011).

For wind forcing of NI IW, a slab model was conducted as in D'Asaro (1995) and Alford (2001), providing a simplified idea of the ML response to NI wind forcing (Alford et al., 2016). Though simple, the model is continuously being improved to better account for non-homogeneous internal ML processes, and ML to pycnocline energy transfer (Alford and Zhao, 2007; Jarosz et al., 2008; Alford et al., 2016; Zheng et al., 2017; Voelker, 2020; Alford, 2020). From surface wind time series, wind stress is calculated as in Garratt (1977):

$$\tau_0 = \rho C_D V(z)^2 \quad (12)$$

where  $\rho$  is the density of air (approximated as 1),  $V(z)$  is the complex wind velocity vector, and  $C_D$  is the characteristic drag coefficient determined by:

$$C_D \times 10^3 = 0.51V^{0.46} \quad (13)$$

For appropriate seasonally, a ML of seasonally varying depth,  $H$ , must be considered. Assuming a null initialisation parameter  $u_{I1}$  at time  $t_1$ , wind

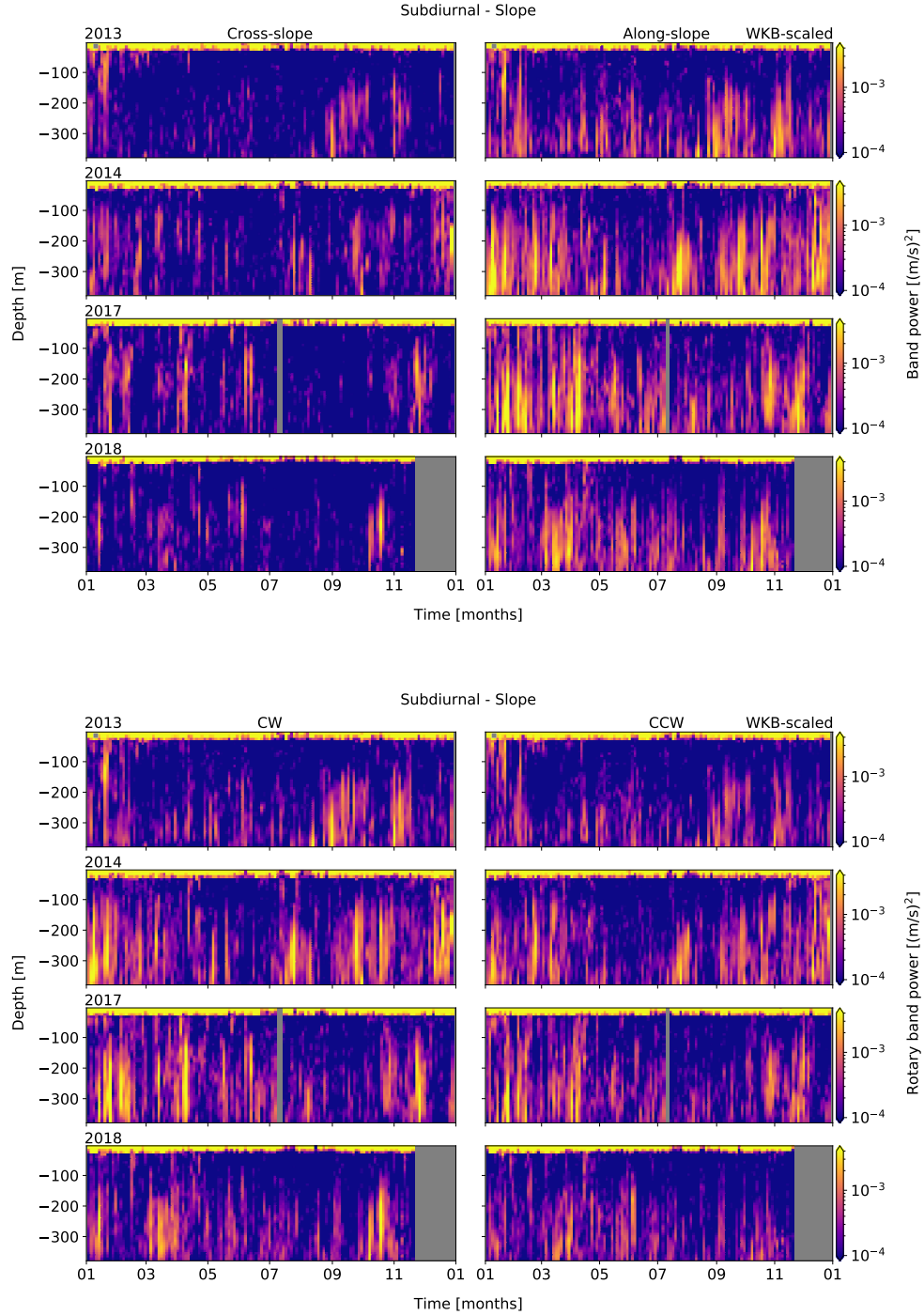


**Figure 15.** Band-integrated sub-diurnal PSD (upper) and rotary (lower) spectra for Slope, from WKB-scaled horizontal velocity data. Cross- (left) and along-slope (right) components are shown. Each row represents an analysis year, labelled at upper-left.

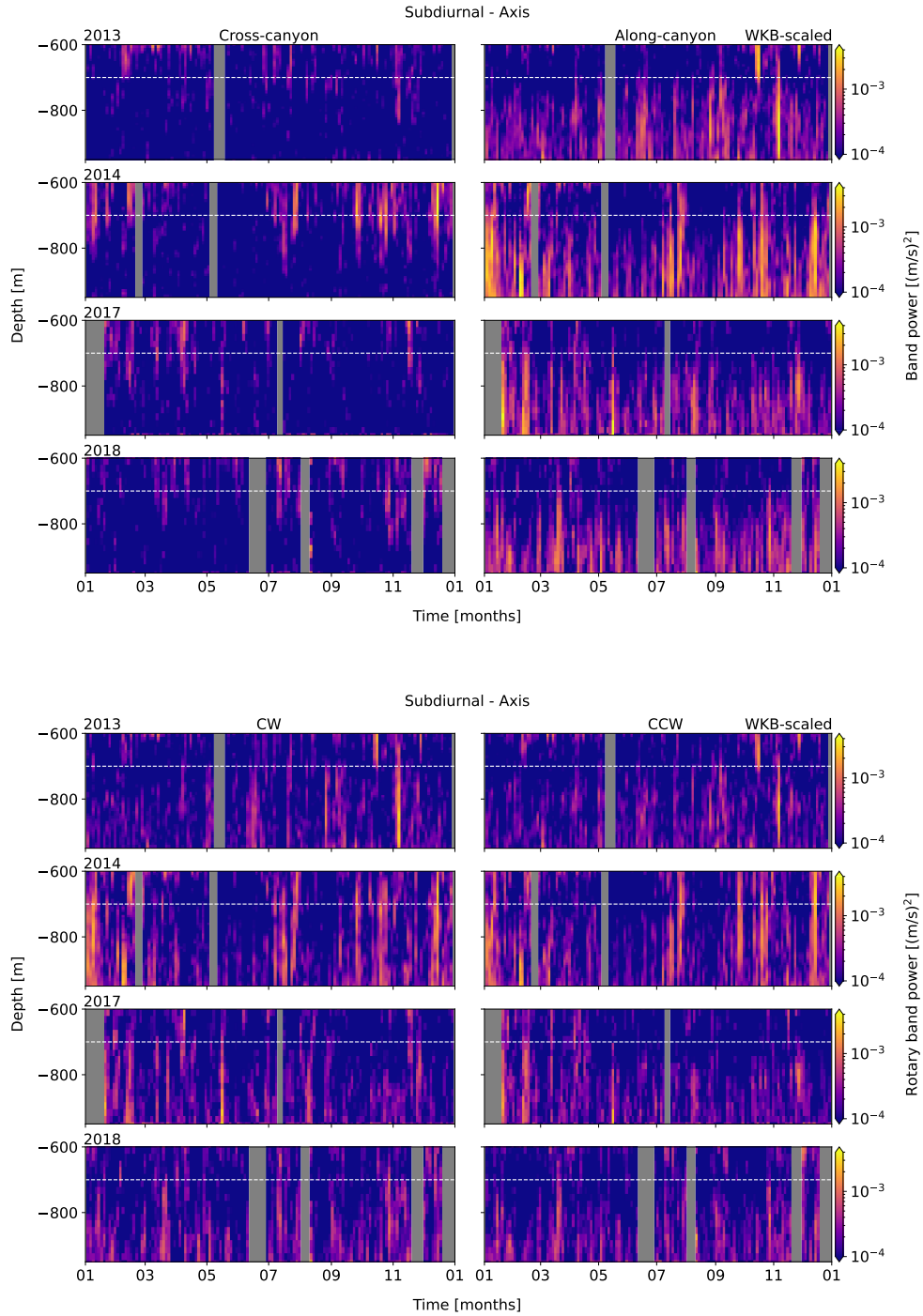


**Figure 16.** Band-integrated sub-diurnal PSD (upper) and rotary (lower) spectra for Axis, from WKB-scaled horizontal velocity data. Cross- (left) and along-slope (right) components are shown. Each row represents an analysis year, labelled at upper-left.

generated slab layer currents at time  $t_2$  are then computed as:

$$u_{I2} = u_{I1}e^{-\omega\Delta t} - \frac{T_t}{H\omega^2}(1 - e^{-\omega\Delta t}) \quad (14)$$

where a damped rotation frequency,  $\omega$ , is determined as:

$$\omega = r + if \quad (15)$$

with  $r = 0.15f$  as an artificial damping parameter, as defined in Alford (2001); and

$$T_t = \frac{\Delta T}{\Delta t} \quad (16)$$

is related to the complex stress vector, defined as:

$$T = \frac{\tau_x + i\tau_y}{\rho_{ML}} \quad (17)$$

where  $\rho_{ML} = 1024 \text{ kg/m}^3$  is the average density of the ML. The slab currents are then band-passed for their NI component,  $u_{NI}$ .

## 6 Results

### 6.1 Observations

#### 6.1.1 Mean currents

Regional low-frequency mean currents are inter-annually consistent, topographically guided, and seasonally site-dependent (Figure 9). To identify long-term mean currents, a 40-hour, 8th-order, digital low-pass Butterworth filter was applied to the WKB-scaled horizontal velocity data. There is little inter-annual variability in mean currents. At Slope, mean currents below -50 m are as expected for this portion of the California current system (Figure 9): generally poleward along-slope (up to  $> 0.2 \text{ m/s}$ ) through depth, with a quick transition to upwelling-favourable equatorward flow in the late-spring (April/May), with the deep poleward currents shoaling by fall (Thomson et al., 2015).

In the canyon, mean currents below -700 m are consistently up-canyon (up to  $> 0.05 \text{ m/s}$ ), with down-canyon flow  $< 50 \text{ m AB}$  (Figure 10). A two-week rolling depth-average between -700 and -900 m yields consistently positive (up-canyon) velocities up to  $0.02 \text{ m/s}$ , with annual means of  $0.007 - 0.010 \text{ m/s}$ . Two-month snapshots show the up-canyon flow is comprised of shoaling pulses with periodicity of about a week. Shoaling is consistent seasonally and inter-annually (not shown).

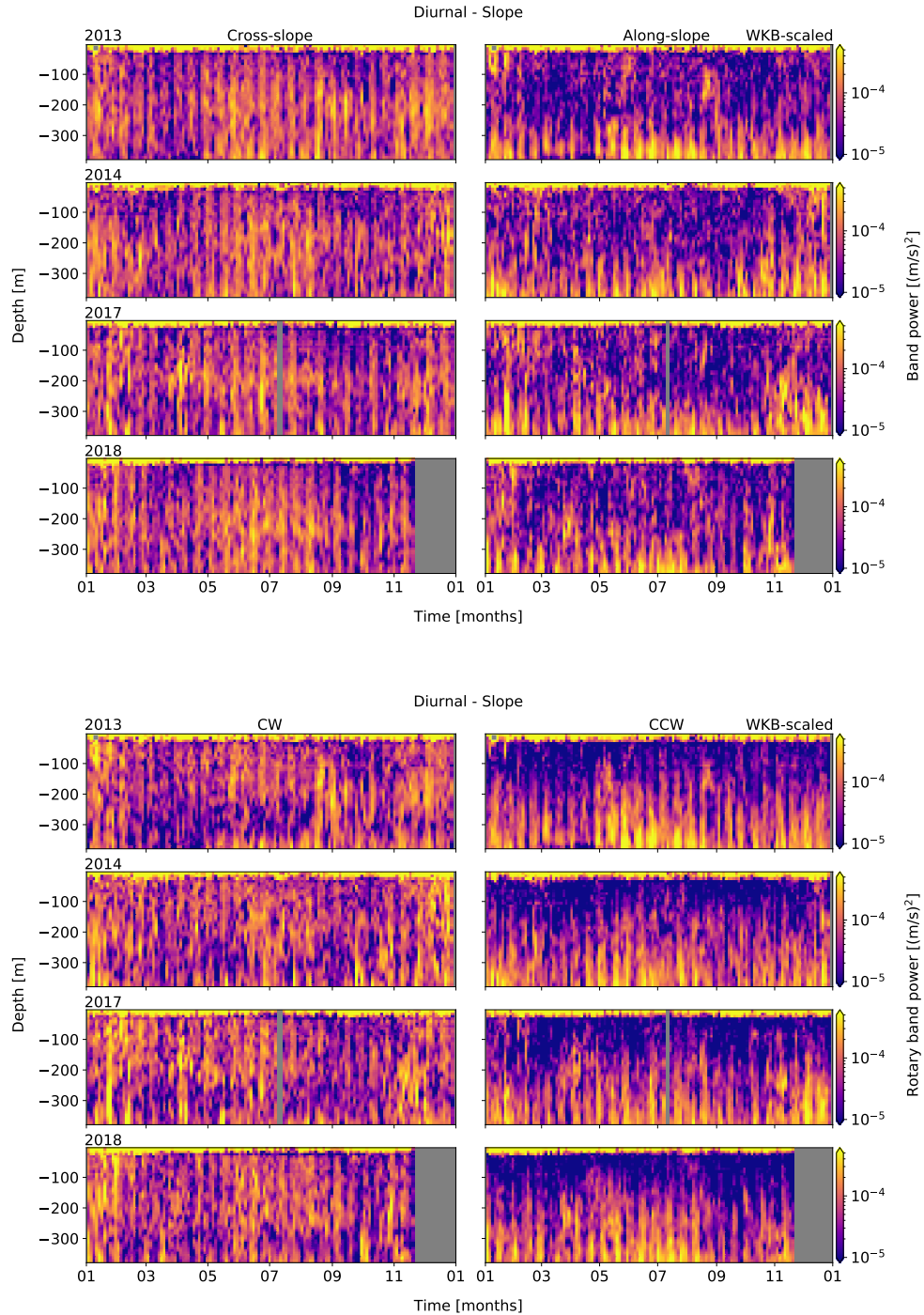


**Figure 17.** Band-integrated diurnal PSD (upper) and rotary (lower) spectra for Slope, from WKB-scaled horizontal velocity data. Cross- (left) and along-slope (right) components are shown. Each row represents an analysis year, labelled at upper-left.

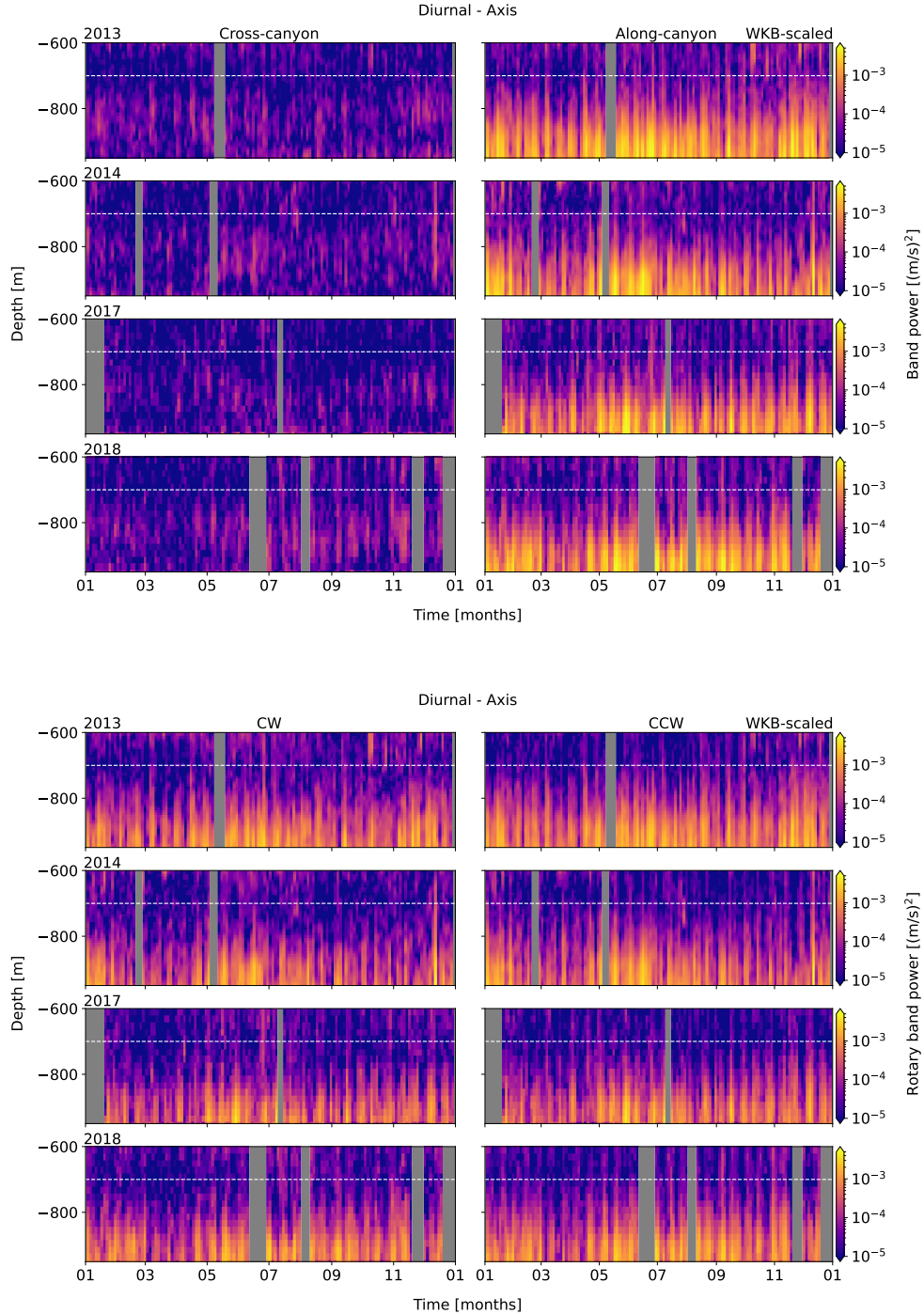


**Figure 18.** Band-integrated diurnal PSD (upper) and rotary (lower) spectra for Axis, from WKB-scaled horizontal velocity data. Cross- (left) and along-slope (right) components are shown. Each row represents an analysis year, labelled at upper-left.

### 6.1.2 High frequency currents

High-frequency (< 40-hour) velocity data show variability in IW and IT. Subtracting the 40-hour low-pass currents from the total yields residual high-frequency currents - flows with periodicity less than 40-hours (Figure 11). A two-week snapshot during the annually recurring April/May mean current transition reveals the presence of IW and IT of various frequencies and non-uniform vertical structure. At the Slope site, high frequency currents reach over 0.1 m/s in both cross- and along-slope directions, and there is shoaling above -250 m depth (about 150 m AB). At Axis, high-pass currents are strongest below -750 m (about 250 m AB), up to about 0.2 m/s and mostly along-canyon, with increased non-uniformity in the vertical structure above.

Annual mid-depth (-195 m and -800 m) power spectra of the high frequency currents at each site show strong tidal and NI influence (Figure 12). Inter-annual variability is minimal (each line of the same colour is a different year), with annual spectra overlapping within the 95% confidence interval. The low-frequency sub-diurnal broadband ranges below  $1.00 \times 10^{-5}$  Hz. The most defined spectral peaks are of the diurnal ( $1.16 \times 10^{-5}$  Hz), NI ( $1.73 \times 10^{-5}$  Hz), and semidiurnal ( $2.24 \times 10^{-5}$  Hz) frequencies. Closely associated tidal constituents (such as  $S_2$  and  $M_2$ ) are not resolved due to spectral averaging, so tidal constituents are referred to generally (e.g. diurnal). The high-frequency IW continuum band ( $7.00 \times 10^{-5} - 1.20 \times 10^{-4}$  Hz) ranges between the  $M_6$  spectral sum peak and the near- $N$  spectral shoulder ( $2.00 \times 10^{-4} - 1.00 \times 10^{-3}$  Hz).

At Slope, the mid-depth power spectra are similar to previous observations on the VICS (Thomson et al., 1990; Allen et al., 2001). The sub-diurnal broadband is strongest along-slope, with strength increasing inversely to frequency. The diurnal constituent is strongest cross-slope (up to  $1.5 \times 10^2$   $\text{m}^2\text{s}^{-2}\text{Hz}^{-1}$ ). The NI peak is of similar strength in both directions (up to  $1.5 \times 10^2$   $\text{m}^2\text{s}^{-2}\text{Hz}^{-1}$ ). The semidiurnal is strongest along-slope (up to  $2.0 \times 10^2$   $\text{m}^2\text{s}^{-2}\text{Hz}^{-1}$ ). Above the minor sum-frequency peaks ( $fM_2$ ,  $M_4$ , etc.), the continuum is stronger cross-slope, and trails off slightly whiter than the expected open-ocean GM slope of -2. Near  $N$ , the spectral shoulder is evident as a whitening effect, and is better resolved in the raw (2-second) spectra, discussed in Section 6.2.6. The sub-diurnal band is nearly rectilinear, while all other constituents are strongest in the CW rotary component, particularly NI, as expected for the northern hemisphere.

At Axis, sub-diurnal, diurnal, NI, and semidiurnal power all trend toward along-canyon rectilinear motions, while the continuum is directionally even and mostly CW. Compared to Slope, the Axis sub-diurnal range is weaker

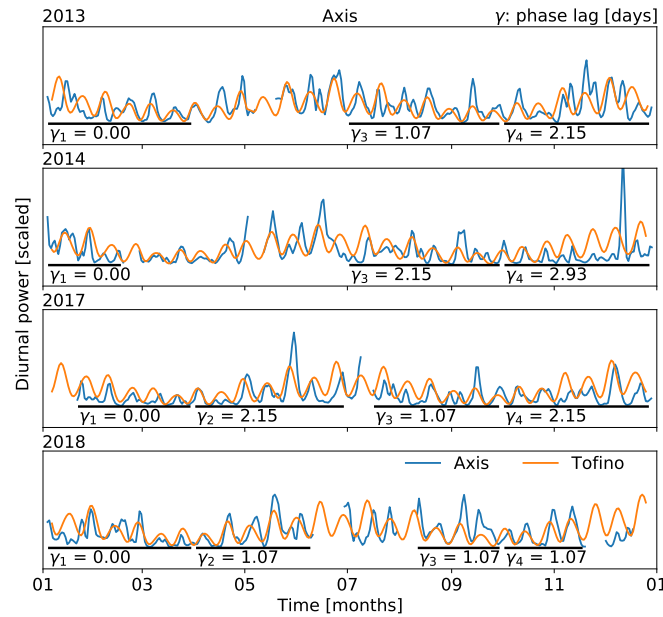
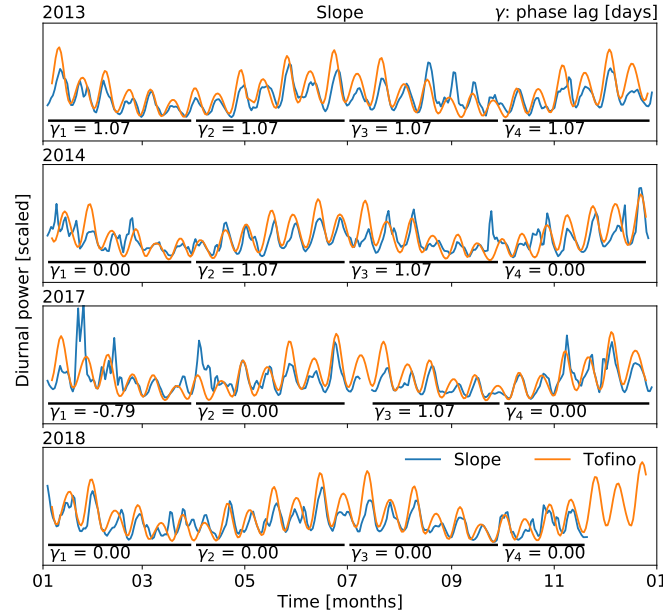


**Figure 19.** Diurnal barotropic forcing comparison. Phase-lag correlation and amplitude (scaled) comparisons for band-integrated power of diurnal surface level data (Tofino, orange) and WKB-scaled depth-mean diurnal power (blue) at Slope (top) and Axis (bottom). Black bars indicate seasonal correlation ranges. There is a consistent yet minor phase-lag, less than the time-scale of each spectral estimate.

at frequencies below  $4.00 \times 10^{-6}$  Hz. The rest of the IW and IT spectrum is slightly more energetic than at Slope, and the near- $N$  spectral shoulder is more pronounced. However, the shoulder is masked in 2017 and 2018 by the Nortek 55 kHz instrument's noise floor.

### 6.1.3 Depth dependence

At each site, there is adjustment of spectral power near topography that is frequency-dependent. The WKB-scaled PSD and rotary spectra were time-averaged for annual 2D depth-frequency analysis (Figures 13 and 14). Results show a general increase (or decrease, for NI at Slope) in spectral power (over an order of magnitude) in a concentrated layer < a few hundred metres above bottom (AB). The depth dependence of the near- $N$  spectral shoulder will be discussed in Section 6.2.6.

At Slope (Figure 13), the sub-diurnal, tidal, and continuum bands show near-slope intensification (while in contrast the NI band is attenuated near the slope) below an average depth of -250 m (130 m AB). Adjustment is up to  $2\times$  orders of magnitude. For the broadband sub-diurnal range, intensification is mostly along-slope and CW. The diurnal intensification is mostly along-slope and CCW. The along-slope sub-diurnal and diurnal observations are typical of sub-inertial frequencies (Flather, 1988). The NI near-slope attenuation is entirely CW. The semidiurnal intensification is mostly along-slope and strongly CW. Continuum intensification is mostly cross-slope and CW.

At Axis (Figure 14), most constituents show rectilinear, along-canyon near-bottom intensification, below an average depth of -750 m depth (230 m AB). Adjustment is up to  $3\times$  orders of magnitude. The sub-diurnal, diurnal, and NI intensification is entirely along-canyon, with little to no power in the cross-canyon direction. The NI band, in contrast to Slope, has bottom-intensified flow that is almost entirely along-canyon. The semidiurnal intensification is strongly along-canyon, but with a medium-strength cross-canyon signal that is sharply attenuated below -900 m. While the semidiurnal along-canyon and CCW components are vertically linear, the weaker cross-canyon and CCW components non-uniform vertical structure. Continuum intensification is directionally even and CW.

A vertical scale analysis roughly agrees with the qualitative observations of enhanced layer thickness. Gemmrich and Klymak (2015) found that mode-1 IW incident on sloped topography can induce a near-bottom turbulent flow layer, and that the vertical scale of the effect can be approximated as:

$$H \approx \frac{\pi U}{N} \quad (18)$$

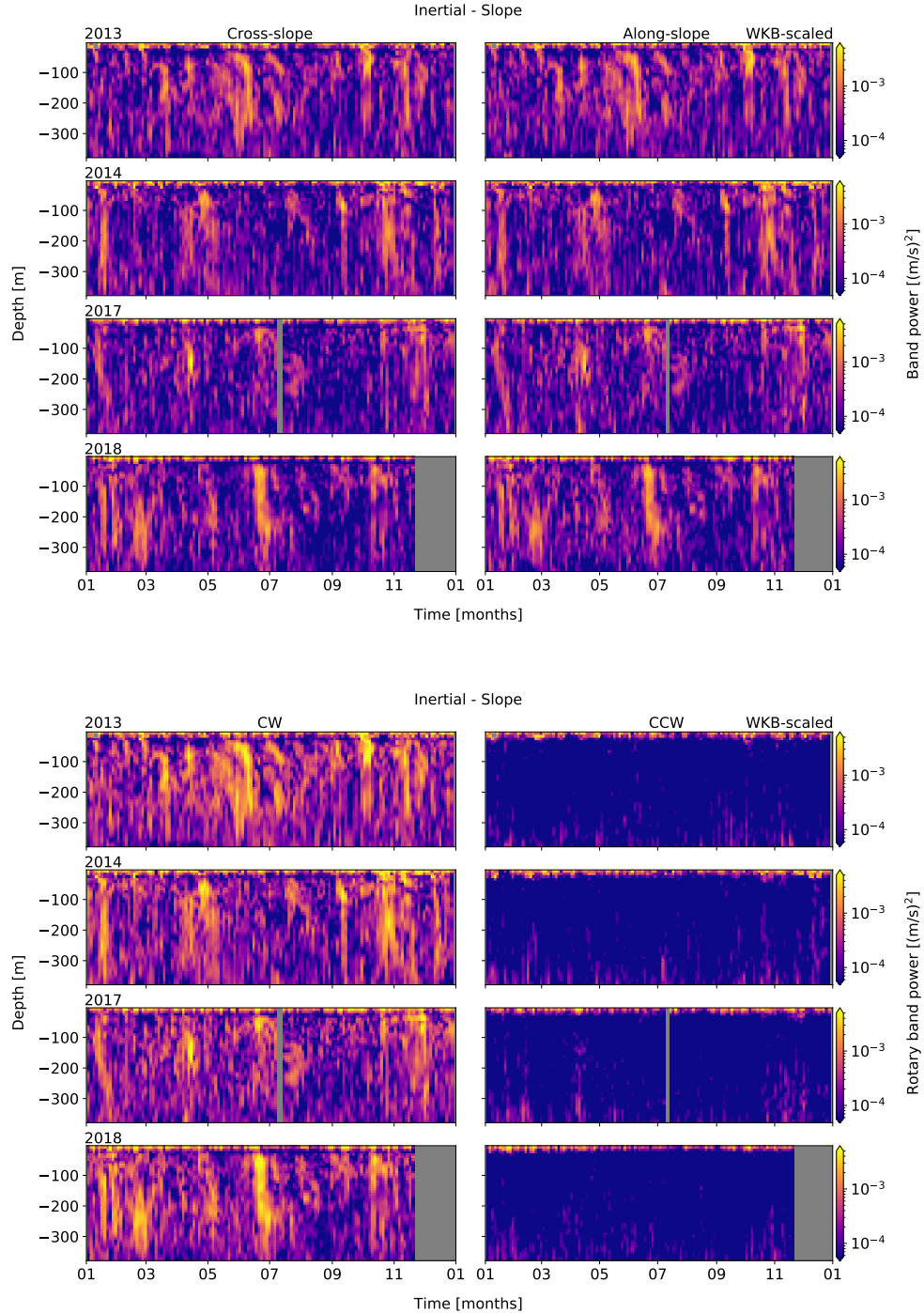


**Figure 20.** Band-integrated NI PSD (upper) and rotary (lower) spectra for Slope, from WKB-scaled horizontal velocity data. Cross- (left) and along-slope (right) components are shown. Each row represents an analysis year, labelled at upper-left.

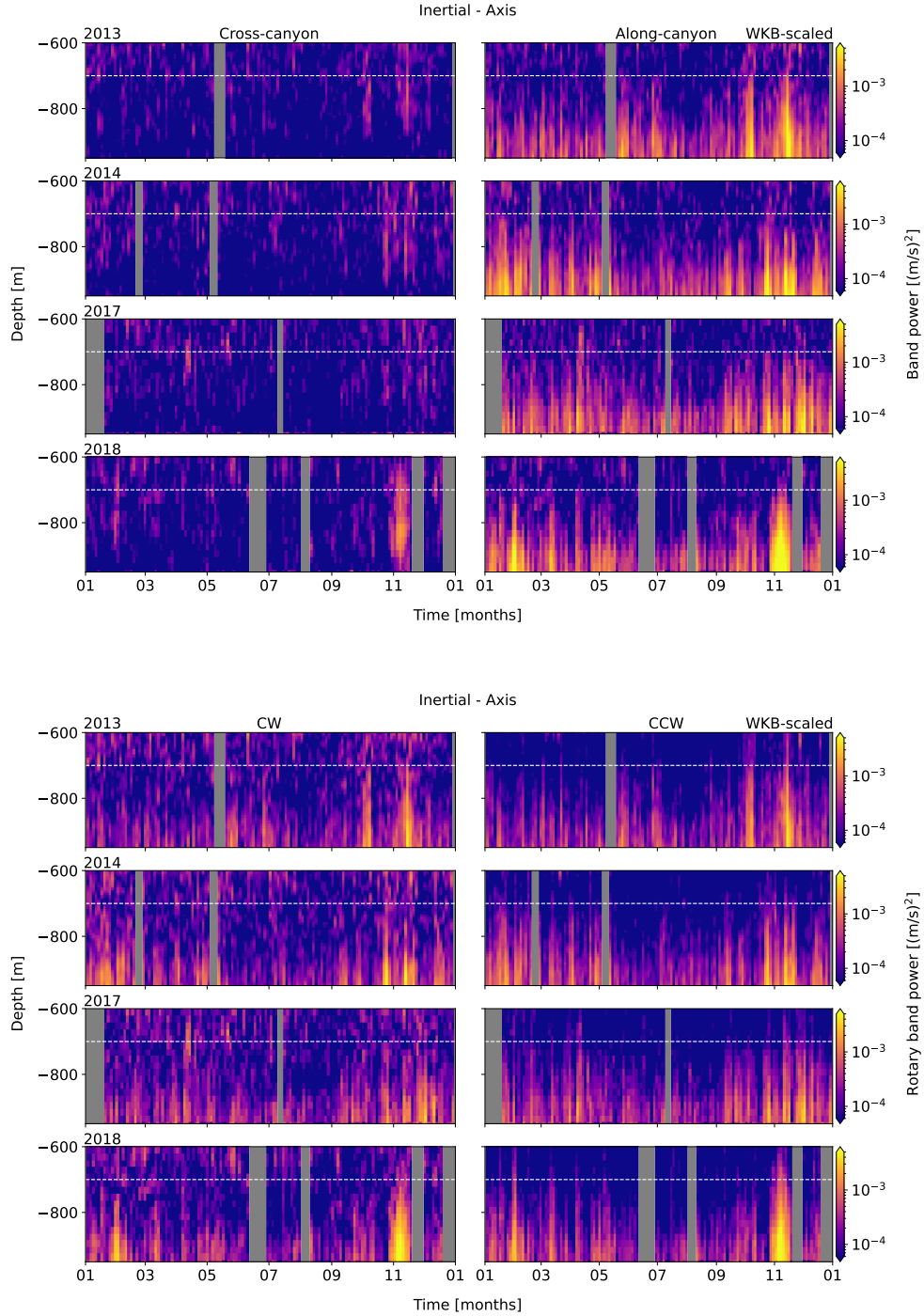


**Figure 21.** Band-integrated NI PSD (upper) and rotary (lower) spectra for Axis, from WKB-scaled horizontal velocity data. Cross- (left) and along-slope (right) components are shown. Each row represents an analysis year, labelled at upper-left.

where  $U$  is the forcing by horizontal velocity. For strong near-bottom velocities (Figure 11) and approximate buoyancy values (Figure 8) for near-topography depths at Slope ( $U \approx 0.15 \text{ m/s}$ ;  $N \approx 3.5 \times 10^{-3} \text{ rad/s}$ , at -350 m) and Axis ( $U \approx 0.25 \text{ m/s}$ ;  $N \approx 2.5 \times 10^{-3} \text{ rad/s}$ , at -900 m), estimates yield vertical scales of 135 m and 314 m, respectively. Results are similar to the qualitative thickness of 130 m AB at Slope, somewhat greater than the observed 230 m AB at Axis, and agree with the results of Gemmrich and Klymak (2015) for similar forcing and stratification. However, it should be noted that CTD climatology data are from a nearby open-ocean site, and so do not reflect changes in stratification near topography.

## 6.2 Frequency-dependent response

There is frequency-dependent variability in the seasonality of the near-topography enhancement layer (and attenuation for NI at Slope). Little inter-annual variability is observed, noted only in the more intermittent sub-diurnal and NI seasonality. WKB-scaled PSD and rotary spectra were integrated over bandwidths comprising each constituent's peak or frequency range (shown as shaded green in Figure 12), for each depth bin, yielding 2D estimates of depth-band power. Constituent frequency ranges are sub-diurnal ( $\leq 1.08 \times 10^{-5} \text{ Hz}$ ), diurnal ( $1.08 - 1.30 \times 10^{-5} \text{ Hz}$ ), NI ( $1.52 - 1.95 \times 10^{-5} \text{ Hz}$ ), semidiurnal ( $2.17 - 2.39 \times 10^{-5} \text{ Hz}$ ), continuum ( $7.00 \times 10^{-5} - 1.20 \times 10^{-4} \text{ Hz}$ ), and shoulder ( $2.00 \times 10^{-4} - 1.00 \times 10^{-3} \text{ Hz}$ ).

### 6.2.1 Sub-diurnal

At Slope, sub-diurnal enhancement layer seasonality consists of intermittent pulses, strongest in fall and winter, and is one of few observations that is not inter-annually consistent (Figure 15). At Axis, seasonality is weak, showing an occasional fall or winter pulse (Figure 16). There are few seasonal features common to the sub-diurnal depth-band and observed mean currents (Figure 9), or any other constituent. Low-frequency motions can be affected by a variety of physical processes near slope, shelf, and canyon topography (Cummins, 2000), and a forcing analysis for the sub-diurnal range is beyond the scope of this paper.

### 6.2.2 Diurnal

Diurnal enhancement seasonality at Slope (Figure 17) is inter-annually consistent, with a regular pulse late-spring through summer (months 5 - 8) and a weaker pulse in the fall/early-winter (months 11 - 1). Seasonality at Axis is not readily apparent (Figure 18).

Depth-mean diurnal power is consistently in-phase with the local barotropic diurnal spring-neap cycle, fortnightly and seasonally, with minimal phase-lag

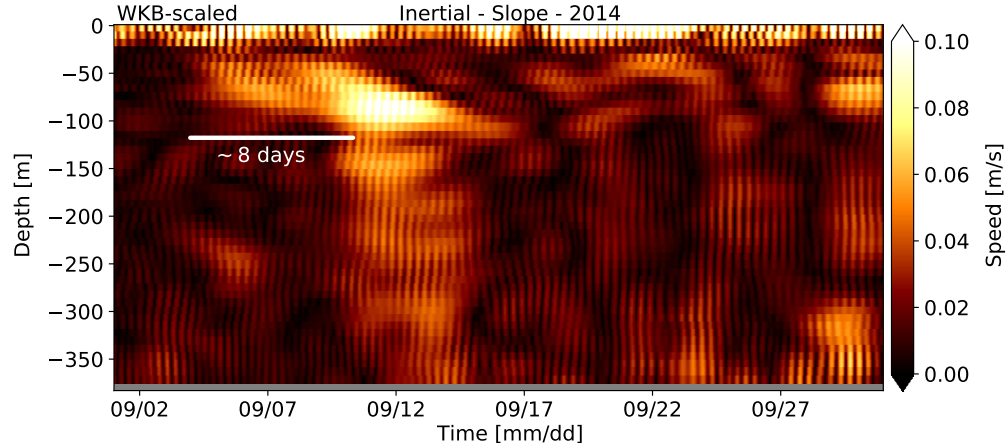


**Figure 22.** Transfer of NI energy in band-passed NI velocity (total) for September, 2014. A wind event excites NI energy in the ML around September 9. Energy is transferred down to about -100 m over about 8 days, after which there is a deep response.

correlations and comparable seasonal scaled amplitudes (Figure 19). Surface-level data were obtained from the Canadian Hydrographic Service (CHS) operated gauge in Tofino, approximately 90 km due north of Barkley Canyon, as hourly time-series of deviation from chart datum, with power spectra diurnally band-passed using the same process as for observations. Comparing long-term seasonality, the Tofino barotropic spring-neap amplitudes peak in months 6-8 and 11-2, corresponding well with the diurnal observations, and consistent inter-annually. Fortnightly, 3-month phase-lag correlations were performed between the depth-mean diurnal power and nearby surface level time series, for months 1-3, 4-6, 7-9, and 10-12, each year. Phase-lag correlations range from 0 to 1 day at Slope (inter-annual average of 0.5 days), and 0 to 2 days at Axis (inter-annual average of 1.1 days) - both less than the time-resolution of the spectral estimates ( $\sim 2.7$  days) used for correlations. It should also be noted that Axis estimates are only partial-depth and cannot fully resolve barotropic water-column motions, potentially contributing to observed phase offsets.

### 6.2.3 Near-inertial

At Slope, NI seasonality above the attenuation region is highly intermittent, with pulses occurring most likely in the fall and early-winter, though possible year-round (Figure 20). At Axis, generally only significant fall and early-winter events from Slope are evident (Figure 21). Seasonality is inter-annually consistent, but specific events are not.

For prominent pulses at Slope, there are periods of downward propagation

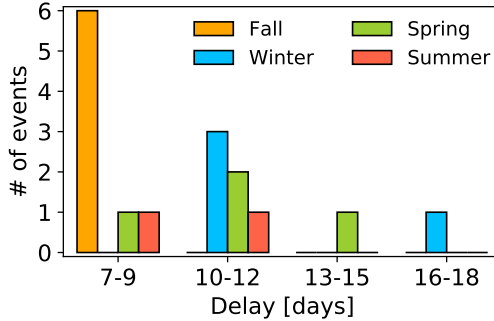


**Figure 23.** Histogram of delayed NI events. Delayed NI deep response events are most common and short-lived in the fall, least common in summer, and longest in the winter.

of NI energy from the ML (above -50 m) to about -100 m, lasting up two weeks, after which the deep response increases quickly. At Axis, the timing of observed pulses appears to correspond to the delayed deep response at Slope. Figure 22 shows a sample event in September, 2014. An event (likely wind, to be discussed), deposits energy into the ML on September 3. Over the next 8 days, energy is transferred down to about -100 m. Upon reaching this depth, there is an immediate deep response. Energy continues to pool around -100 m, maintaining the deep response until September 14, when NI energy appears to have dissipated. There are many of these events each year, recorded in Figure 23. The fall sees the most events, all of which are short lived, from 7-9 days, while the winter has the longest events, up to 16-18 days.

Slab model results indicate NI forcing is qualitatively linked with regional wind events in the fall and early-winter (Figure 24). Wind data were obtained from the closest Fisheries and Oceans Canada (DFO) weather buoy, La Perouse (46206, 50 km N), as time series of magnitude and direction. Regional seasonally varying ML depth,  $H$ , is defined by Thomson and Fine (2003) and Li et al. (2005) for nearby (35 km NW) Line P Station 3; the ML is thick in winter and spring (down to about -60 m), and thinnest summer through early-fall (up to about -20 m). There are large wind data gaps during later years (2014, 2017, and 2018), so 2013 is used as the sample year. Results for later years are available in Appendix A (Section 9). Results yield time series of NI ML currents exceeding 0.1 m/s that are qualitatively similar to wind data, most notably in the fall and early-winter. However, not every event that shows up in the ML is evident in the NI depth-band observations.

Seasonal slab model correlations with NI depth-band power suggest interior NI response to wind forcing is strongest in summer and fall (not shown). To

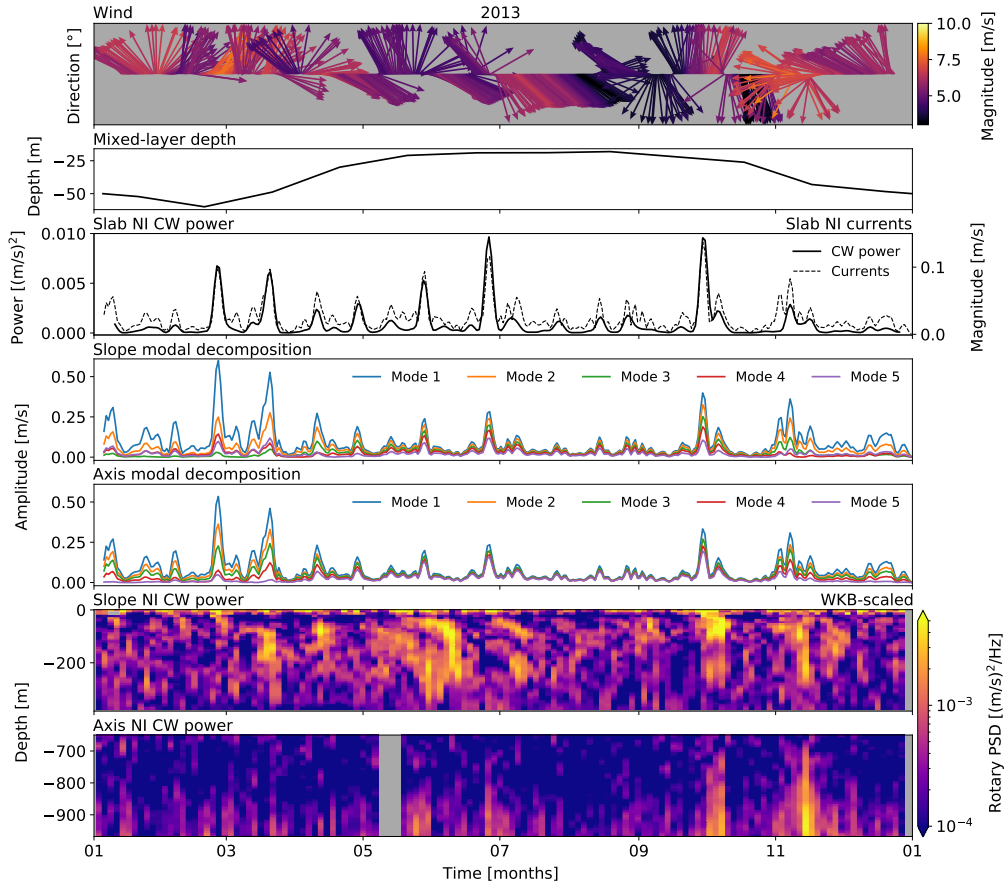


**Figure 24.** NI forcing analysis for 2013. Panels are (i) wind direction and amplitude, (ii) monthly-averaged ML depth for Line P station 3 as determined by Li et al. (2005), (iii) slab model NI CW power and NI currents, (iv, v) seasonal mode amplitudes for Slope and Axis, and (vi, vii) band-integrated NI CW power at Slope and Axis. There appears to be a complex relationship between the wind, ML, slab currents, and mode amplitudes in driving the NI observations, with the most obvious effects in the fall. Due to significant data gaps, plots for other analysis years are in Appendix A (9).

better quantify wind forcing of NI depth-band power, seasonal correlations were obtained similarly to diurnal spring-neap forcing. Correlation estimates were initially poor; the apparent delay in the deep response may affect correlation with the quicker slab response. To cope, a 2-month rolling average was applied to each time-series and relaxed until correlations began to devolve. Ideal rolling average intervals were found to be 3-weeks for the slab data,

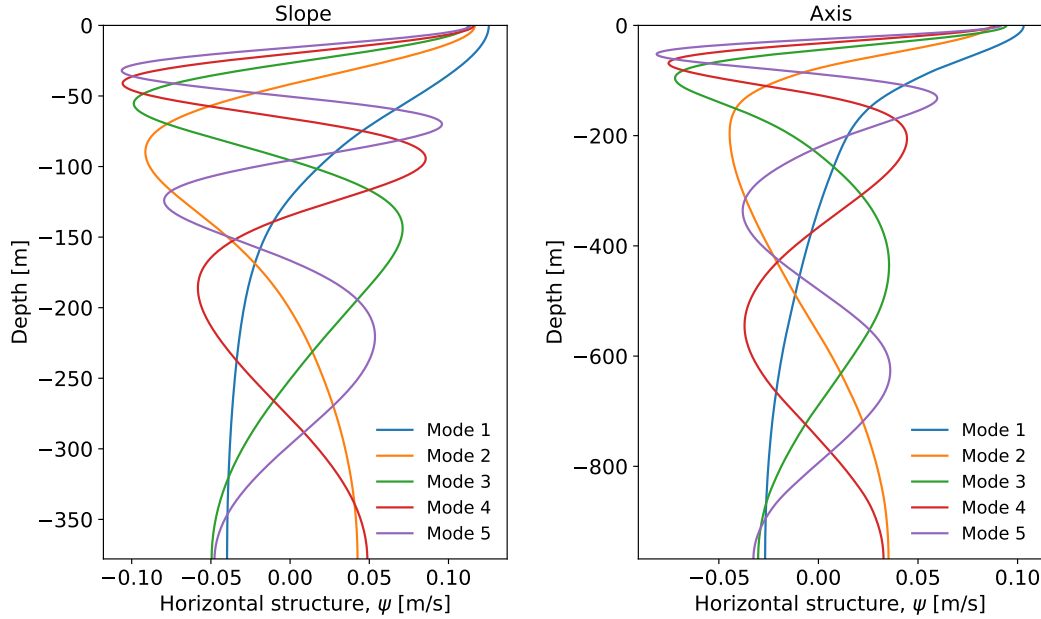


**Figure 25.** Vertical mode decomposition. Depth-dependent horizontal structure of mode amplitudes, for Slope (left) and Axis (right). Mode structure is dependent on site depth and the local stratification profile.

and 1-week for site observations, as the wind data were more highly variable to begin. At Slope, correlations are strong-positive in the fall, and weak- to medium-positive in summer. At Axis, correlations are strong-positive in summer, and weak- to medium-positive in fall. Seasonal correlations are otherwise inconsistent. The fall and summer correlation periods encompass notable wind events that occur while the ML is thin, and there is a more notable response at depth.

Seasonal vertical mode amplitudes suggest high-mode contributions lead to greater NI deep response (Figure 25). For NI IW generation by the NI ML currents, the stratification-dependent vertical mode structure is determined as described in Section 3. When the ML is thin, contributions from low modes (1 and 2) and high modes (3, 4, 5) are about equal ( $\sim 52\%$  low modes); when the ML is thick, modes 1 and 2 dominate ( $\sim 74\%$ ). Similar to the slab correlations, there is a greater deep response when the ML is thin and higher modes are equal contributors, such as in the early-fall when strong storms begin to arrive. High modes contribute most in the summer when the ML is thinnest, but there are few storms; yet even weak summer wind events can warrant a deep response. In contrast, there are many strong wind events in winter and spring, but the ML is thick, low modes dominate, and there is little

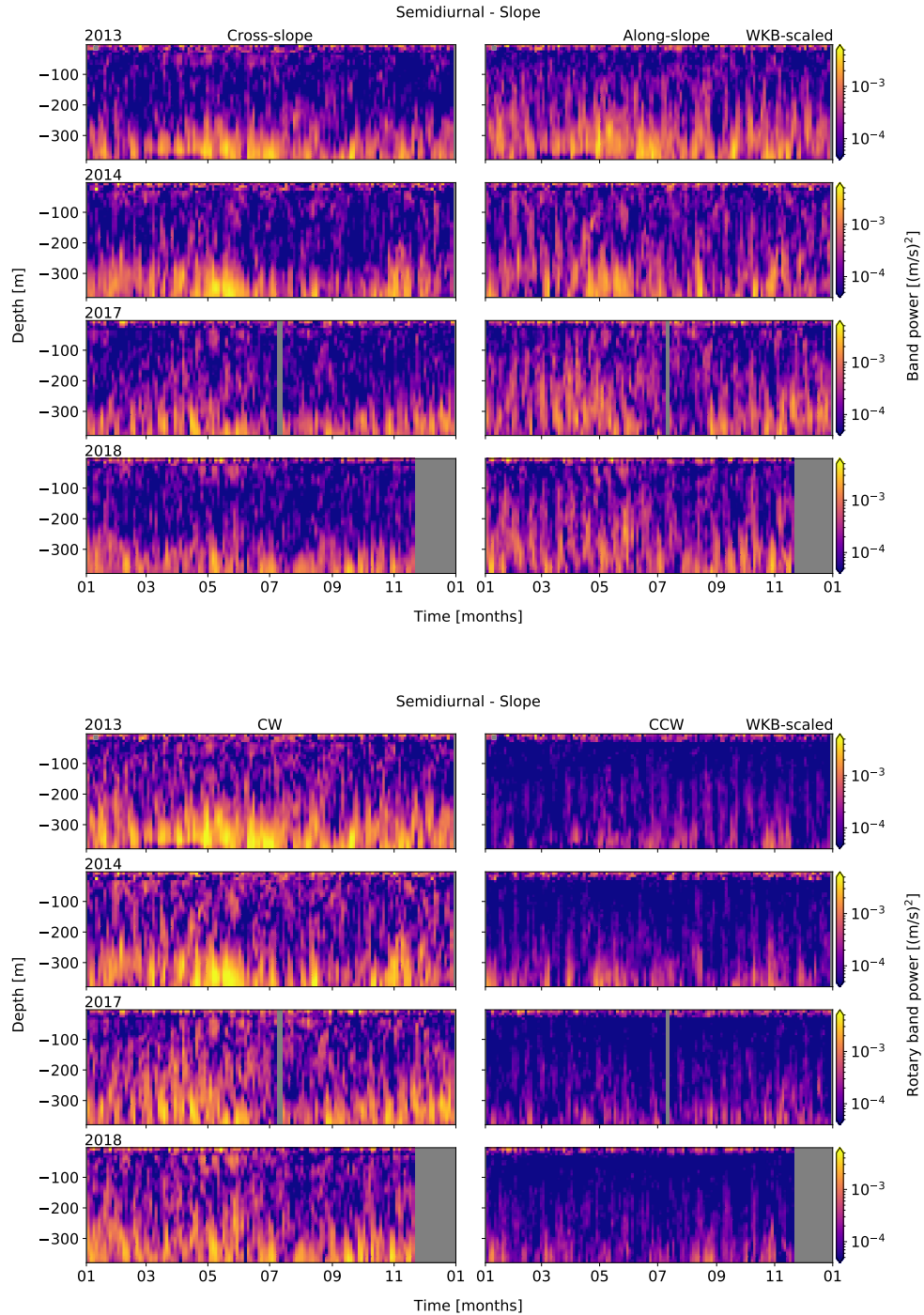


**Figure 26.** Band-integrated semidiurnal PSD (upper) and rotary (lower) spectra for Slope, from WKB-scaled horizontal velocity data. Cross- (left) and along-slope (right) components are shown. Each row represents an analysis year, labelled at upper-left.

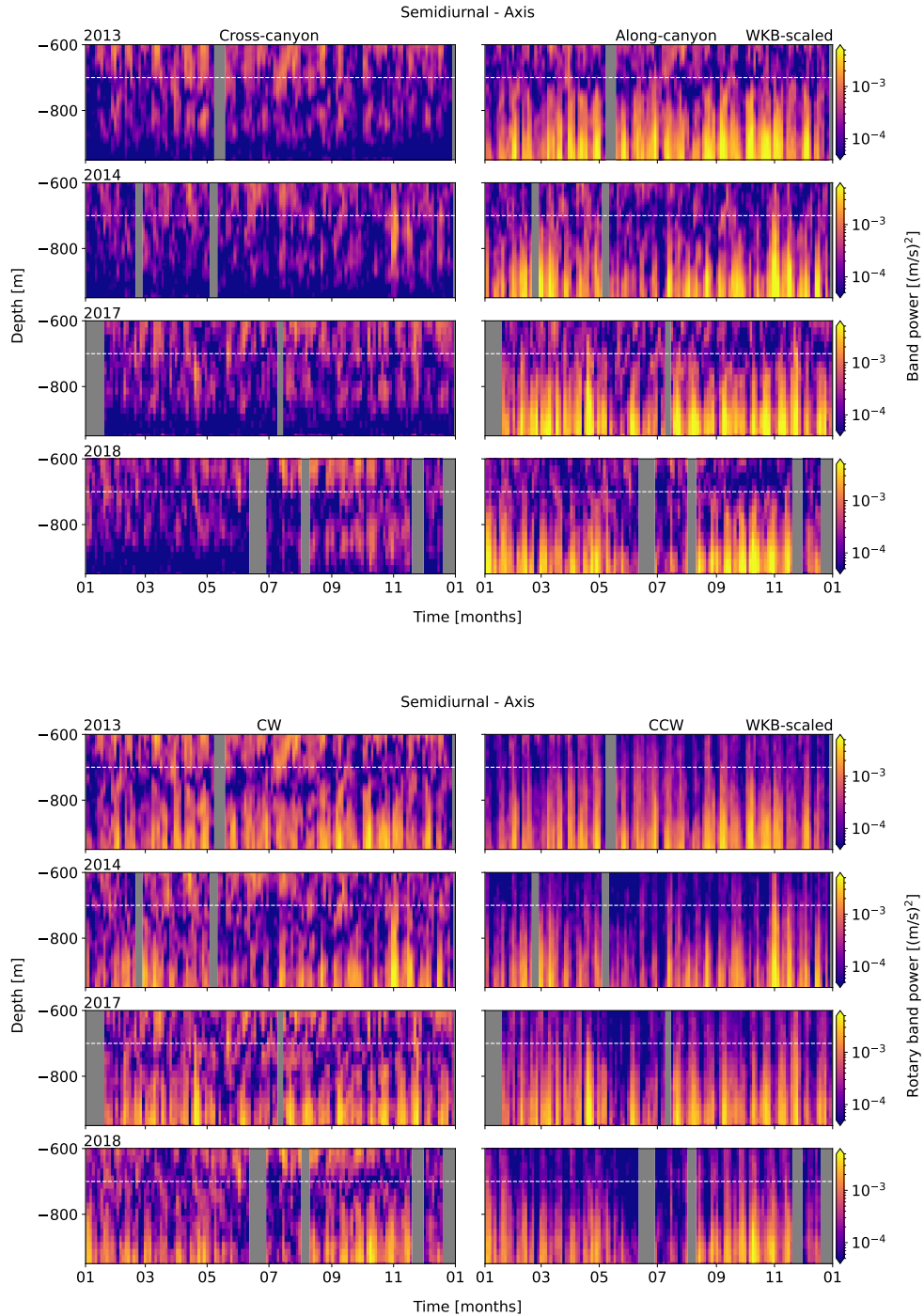


**Figure 27.** Band-integrated semidiurnal PSD (upper) and rotary (lower) spectra for Axis, from WKB-scaled horizontal velocity data. Cross- (left) and along-slope (right) components are shown. Each row represents an analysis year, labelled at upper-left.

or no deep response.

#### 6.2.4 Semidiurnal

Semidiurnal enhancement layer seasonality at Slope is inter-annually consistent and subtle, showing a slight pulse that begins in the late-spring/early-summer (months 4/5) and an even weaker pulse in the fall/early-winter (Figure 26). Seasonality at Axis is not readily apparent (Figure 27).

Semidiurnal barotropic spring-neap forcing is intermittently in-and-out of phase, at both sites (Figure 28). Phase-lag correlations were determined as for the diurnal band. The scaled semidiurnal depth-mean band-power amplitudes vary greatly from the seasonal spring-neap surface levels. Fortnightly phase-lags are inconsistent, and for 3-month periods range from 0 to 4 days at Slope (inter-annual average of 2.3 days), and from 0 to 6 days at Axis (inter-annual average of 2.8 days).

#### 6.2.5 Continuum

Continuum seasonality at Slope is inter-annually consistent, with a pulse in spring through early-summer, and another through the fall (Figure 29). At Axis, seasonality is less apparent, though there is generally more activity in the fall (Figure 30).

Compared to the open-ocean GM spectrum, the observed continuum amplitude is higher, and the slope more negative (Figure 31). For depth-specific time series of WKB-scaled PSD (Slope -300 m; Axis -900 m), a power law of  $af^b$  was fit to the continuum frequency range and smoothed in two week intervals, resulting in a time series of power law amplitude ( $a$ ) and slope ( $b$ ). A similar fit was applied to the open-ocean GM spectrum (half GM, to compare with  $u$  and  $v$  components), to determine values for  $a_{GM,0.5} \approx 2.7 \times 10^{-9} \text{ m}^2\text{s}^{-2}\text{Hz}^{-1}$  and  $b_{GM,0.5} \approx -2.1$ . Observed  $a$  ranges within  $2 - 5 \times 10^{-9} \text{ m}^2\text{s}^{-2}\text{Hz}^{-1}$ , and  $b$  within  $-2.0 - -2.3$ . Time series of power law amplitude and slope are strongly correlated, each a rough copy of continuum depth-mean depth-band power seasonality (not shown).

Continuum energy is depth-dependent near topography, and elevated compared to open-ocean GM energy (Figure 32). The open-ocean GM spectrum was 'whitened' over the continuum frequency range - its power multiplied by  $f^2$  - then averaged to find  $E_{GM} \approx 8.1 \times 10^{-9} \text{ m}^2\text{s}^{-2}\text{Hz}$ . Determined similarly, WKB-scaled continuum energy,  $E_c$ , was compared to  $E_{GM}$  in both depth and time. Results yield non-isotropic  $E_c$  amplitudes up to  $7 \times E_{GM}$ , near topography, while away from topography,  $E_c$  levels fall to equivalent or below that of  $E_{GM}$ .

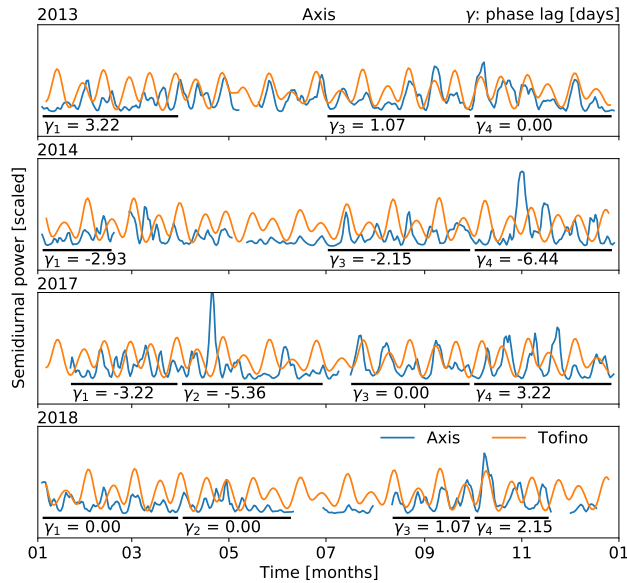
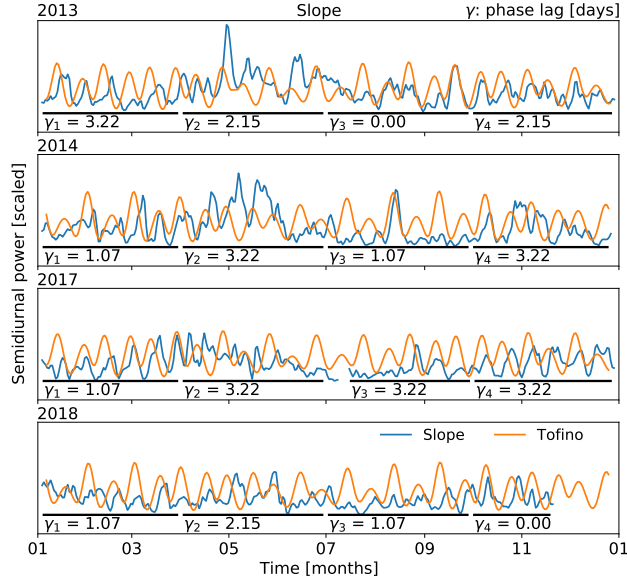


**Figure 28.** Semidiurnal barotropic forcing comparison. Phase and amplitude (scaled) comparisons for band-integrated power of semidiurnal surface level data (Tofino, orange) and WKB-scaled depth-mean semidiurnal power (blue) at Slope (top) and Axis (bottom). Black bars indicate seasonal correlation ranges. Though the instrument amplitude is highly irregular, there is a variable phase lag that suggests a mix of local barotropic and remote baroclinic forcing.

Elevated near-topography continuum energy leads to enhanced dissipation rates,  $\varepsilon$ , at both sites (Figure 33). From IW interaction theory (Althaus et al., 2003), dissipation estimates were calculated from the WKB-scaled  $E_c$  amplitudes as:

$$\varepsilon = \varepsilon_0 \frac{N_0^2}{N_{GM}^2} \frac{\langle E_c^2 \rangle^2}{\langle E_{GM}^2 \rangle^2} f(R_\omega) \quad (19)$$

where  $\varepsilon_0 = 4.1 \times 10^{-11}$  W/kg,  $\langle E_c^2 \rangle^2 / \langle E_{GM}^2 \rangle^2$  is the measured ratio of continuum energy to GM energy over the same frequency range, and the upper bound

$$f(R_\omega) = \left( \frac{R_\omega + 1}{R_\omega} \right)^2 \left[ \text{arc cosh} \left( \frac{N_0}{f} \right) + \frac{25 \text{arc cos}(f/N_0)}{\sqrt{R_\omega}} \right] \quad (20)$$

is an energy ratio as defined by Sun and Kunze (1999), with  $R_\omega = 2.13$  (Kunze et al., 2002) for a continuum with predominantly semidiurnal forcing (to be discussed). Results exceed  $10^{-8}$  W/kg near topography, following continuum seasonality. Away from topography, dissipation is on the order of  $10^{-9}$  W/kg or less.

Turbulent eddy diffusivities,  $\kappa$ , are similarly elevated near topography (Figure 33). From  $\epsilon$ , diffusivity was calculated as by Kunze et al. (2002):

$$\kappa = \frac{\gamma \varepsilon}{N_0^2} \quad (21)$$

where  $\gamma = 0.2$  is the mixing efficiency for high-Reynolds-number turbulence. Turbulent eddy diffusivities reach  $10^{-3}$  m<sup>2</sup>s<sup>-1</sup> near topography, and seasonality is again linked to continuum depth-band power. Away from topography, diffusivity values are on the order of  $10^{-5}$  m<sup>2</sup>s<sup>-1</sup> or less, consistent with open-ocean values (Gregg, 1989; Kunze et al., 2002).

Continuum (and therefore dissipation) seasonality is correlated with semidiurnal forcing at both sites, with secondary contributions from the sub-diurnal band at Slope, and the NI band at Axis (Figure 34). First, correlations were determined as for NI wind forcing, for each frequency band. At Slope, the semidiurnal band shows moderate- to strong-positive correlations in the spring, while the sub-diurnal band shows weak- to moderate-positive correlations in both winter and spring. At Axis, the semidiurnal band is strong-positive all year, while the NI band is moderate- to strong-positive in the spring and fall. There is no apparent fortnightly modulation of continuum power or vertical scale associated with diurnal or semidiurnal spring-neap effects. To further quantify these relationships, and assist in estimating dissipation for modelling, power

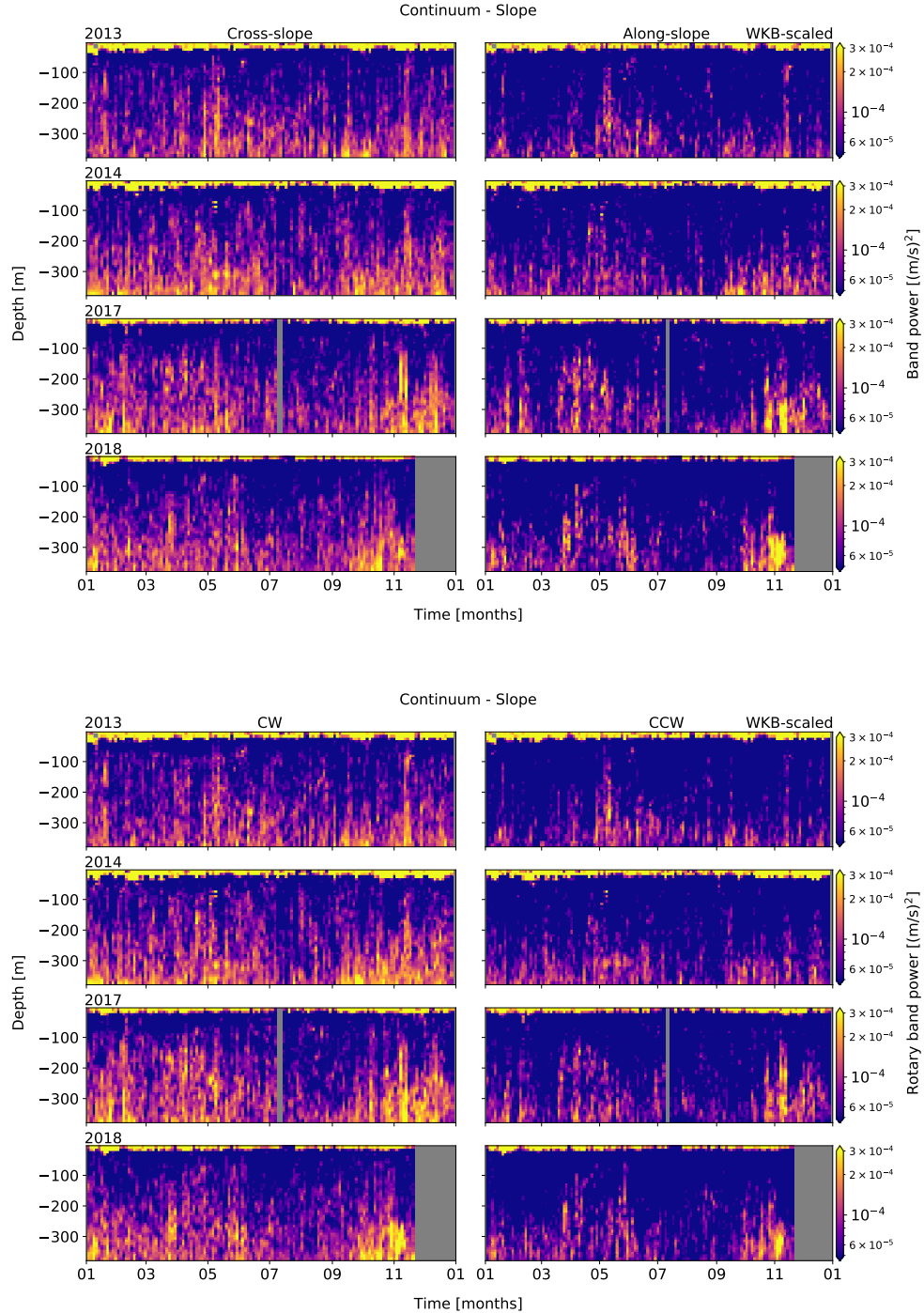


**Figure 29.** Band-integrated continuum PSD (upper) and rotary (lower) spectra for Slope, from WKB-scaled horizontal velocity data. Cross- (left) and along-slope (right) components are shown. Each row represents an analysis year, labelled at upper-left.

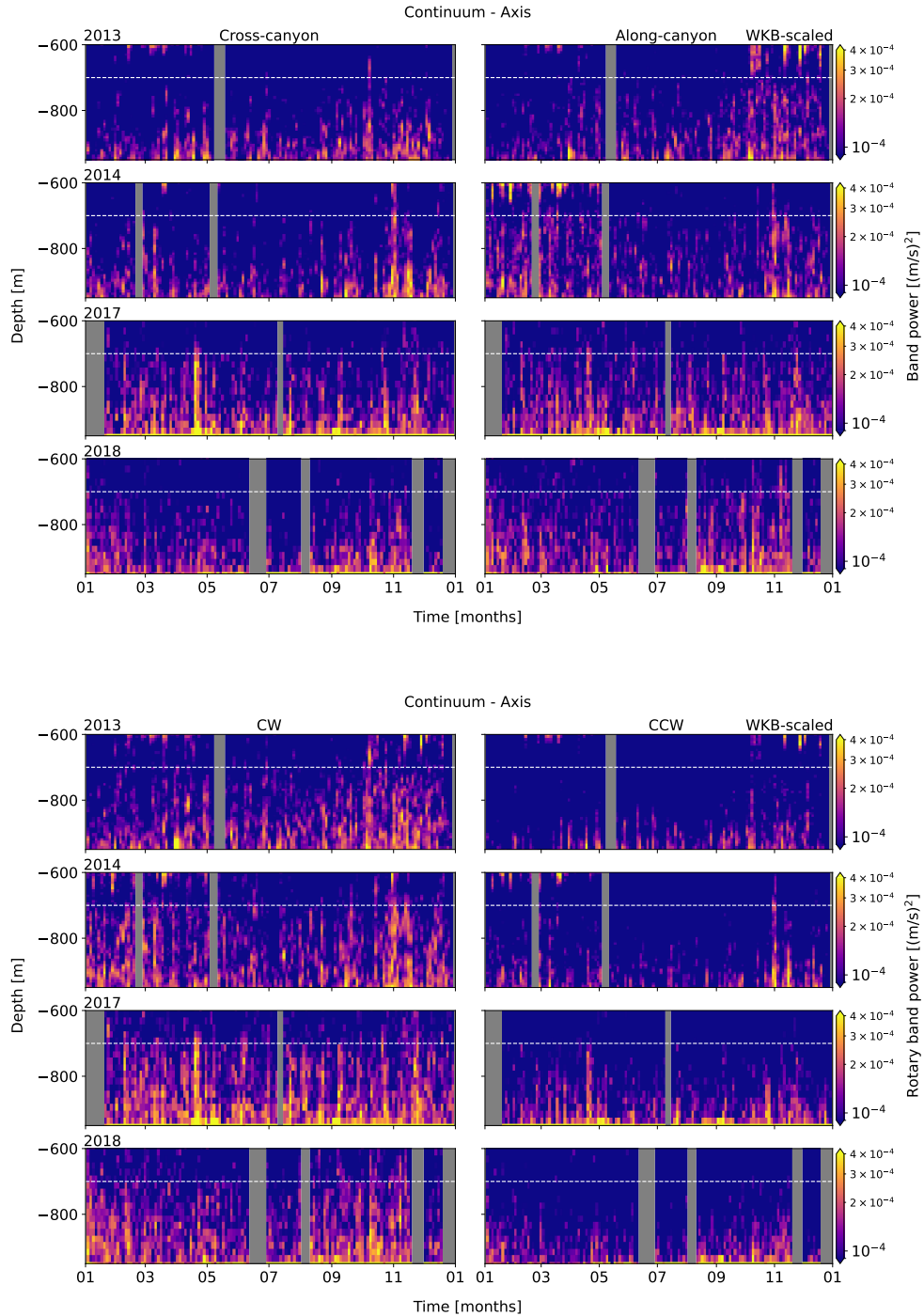


**Figure 30.** Band-integrated continuum PSD (upper) and rotary (lower) spectra for Axis, from WKB-scaled horizontal velocity data. Cross- (left) and along-slope (right) components are shown. Each row represents an analysis year, labelled at upper-left.

laws of  $af^b$  were fit to scatter plots of depth-mean dissipation-power time series, providing estimates of  $a$  and  $b$  for each constituent. The process was then bootstrapped for improved uncertainties. At both sites, the semidiurnal band appears to have the best fit, particularly at Axis. The sub-diurnal band at Slope, and the NI band at Axis, are secondary contributors with less obvious fits. Though both bands contribute to higher dissipation as they increase, they do not drive each other. The power law fits for estimating dissipation are  $\epsilon \sim M_2^{0.42 \pm 0.08}$  at Slope, and  $\epsilon \sim M_2^{0.64 \pm 0.09}$  at Axis.

Multi-variate analysis improves power law fits, reinforcing the importance of the secondary contributing constituents (Figure 35). Secondary constituents were added to the semidiurnal power law of  $ax_1^b + cx_2^d$ , where  $x_1$  is the depth-mean semidiurnal band-power and  $x_1$  is the secondary constituent. This process was also bootstrapped for improved uncertainties. Using the sub-diurnal band as secondary for Slope, and the NI band for secondary at Axis, multi-variate power laws relationships of  $\epsilon \sim M_2^{0.83 \pm 0.33} + \text{Sub}_{K1}^{0.59 \pm 0.27}$  and  $\epsilon \sim M_2^{1.47 \pm 0.48} + \text{NI}^{0.24 \pm 0.06}$  were found for each site, respectively. The multi-variate fits are an improvement over the purely semidiurnal fits, as a percent good metric indicates that for Slope the multi-variate fit is closer to  $\epsilon$  for 68% of data points, and 62% at Axis. If making use of either of these sets of power law relationships, it is important to keep in mind that continuum power alone may not provide a good initial estimate of observable dissipation.

### 6.2.6 Shoulder (incomplete)

The near- $N$  spectral shoulder is typically unresolved in power spectra of oceanographic data, and the 15-minute data used in this study do not fully expose the hump. For analysis of the spectral shoulder, 2-second data from the 75 kHz RDI instruments were obtained to allow for increased Nyquist frequency, and a noise floor low enough to resolve the hump. Shoulder depth-band power does not show clear depth-dependent enhancement near-bottom, as for lower frequency constituents (Figures 36 and 37). At Slope, shoulder power is mostly cross-slope and rectilinear, and intermittent in depth. At Axis, shoulder power is evenly distributed directionally and rotationally, and is more vertically uniform than at Slope. Shoulder seasonality at Slope is subtle, with increased power in the spring and fall. At Axis, there is increased power in only the fall; however, there are multiple issues with interpreting seasonality at Axis. In September 2013 and May 2014 there were maintenance and instrument swaps which affected Axis ADCP deployment parameters, resulting in distinct periods of higher variance (though this does not affect lower frequencies). Furthermore, a switch to a Nortek 55 kHz instrument for 2017 and 2018 does not allow for clear resolution of the spectral shoulder, as the 55 kHz instrument's noise

floor is higher than that of the previous RDI 75 kHz instruments (Figure 12). Regardless of these issues, rough inspection shows that shoulder seasonality is qualitatively similar to the continuum, alone, albeit with additional pulses that are intermittent in time and depth.

There is a distinct power law relationship between dissipation and the spectral shoulder (Figure 38). Power law fits for WKB-scaled dissipation and shoulder depth-band power ( $P_{sh}$ ) were determined as for the continuum analysis in Section 6.2.5. At Slope, there is a reasonable fit of  $P_{sh} \sim \epsilon^{0.36}$ . At Axis, the period of highest variance (September 2013 to May 2014) was neglected, and a power law fit to the remaining 2013 and 2014 data. There are two distinct sets of data, which qualitatively have similar distribution and slope, yet are up to a factor of 2 apart.

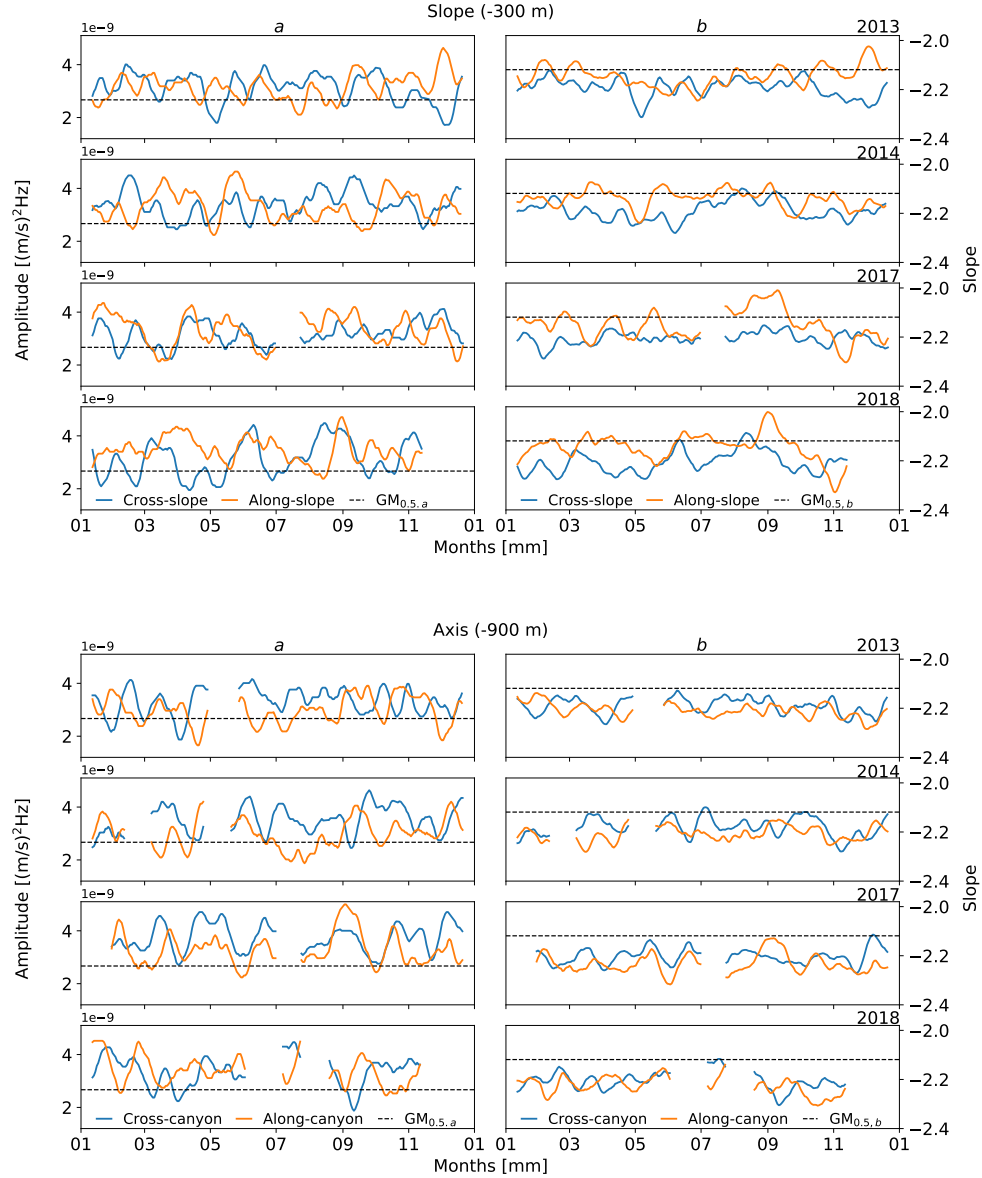


**Figure 31.** Time-series of continuum power law fits. Continuum amplitude,  $a$  (left), and slope,  $b$  (right), of power law ( $a f^b$ ) fits to lower-depth WKB-scaled PSD, at Slope (top) and Axis (bottom). For each site, each row is a year, labelled upper-right. Time series were smoothed over two weeks. Compared to GM, amplitudes are elevated up to  $\times 2$  GM in the centre of the enhancement layer, with slopes down to -2.3.

## 7 Discussion

### 7.1 Axis mean currents

The along-canyon mean flow at Axis is notable for its seasonal and inter-annual consistency and circulation implications, important for understanding sediment transport and physical-biological coupling influencing VICS productivity (Xu and Noble, 2009). In previous biological studies at Barkley Canyon (Cabrera et. al, 2018; Chauvet et al., 2018), a two-layer flow system was noted similar to that of Hudson Canyon (Hotchkiss and Wunsch, 1982) and Monterey Canyon (Xu and Noble, 2009); the systems were attributed to circulation cells caused by along-canyon pressure gradients driven by consistent large-scale quasi-geostrophic along-shelf regional currents. The shoaling of these currents was observed with periodicity ranging from semidiurnal (Monterey Canyon) to  $>$  than a few days (Hudson Canyon), and found to shoal at an angle similar to that of the up-slope gradient (Hotchkiss and Wunsch, 1982; Petruncio et al., 1998; Xu and Noble, 2009). Tidal rectification, where an up-slope pressure gradient is driven by tidal forcing (Garrett, 2005), could force a periodic mean up-canyon flow. Additionally, near-bottom ( $< 50$  m) down-canyon flow could be linked to turbidity currents and river-flood-induced underflows, that occur as shelf sediment descends through canyons to the ocean interior (Xu and Noble, 2009; Chauvet et al., 2018).

To associate observed periodicity with relevant forcing, correlations were run versus Slope mean currents, spring-neap tidal cycles, and depth-averaged semidiurnal depth-band power. Correlations are inconsistent (not shown), and do not suggest forcing by these sources. However, though there is no obvious connection to diurnal or semidiurnal spring-neap forcing, estimates of total lower-canyon transport (bottom to -700 m) from depth- and time-mean annual velocities result in near-zero net up-canyon flow (annually between 0.004 - 0.005 m/s), potentially consistent with tidal rectification theory (Garrett, 2005).

Though along-canyon mean flow systems have been noted at other canyons, the periodicity and attributed forcing comparisons at Barkley Canyon do not align with other sites. It is possible that such circulation may be common in canyons, with unique forcing depending on site characteristics and regional physical processes.

### 7.2 Tidal forcing

The diurnal and semidiurnal tidal constituents are two of the greatest sources of IW energy, and affect mean currents, mixing, IT and baroclinic shelf wave

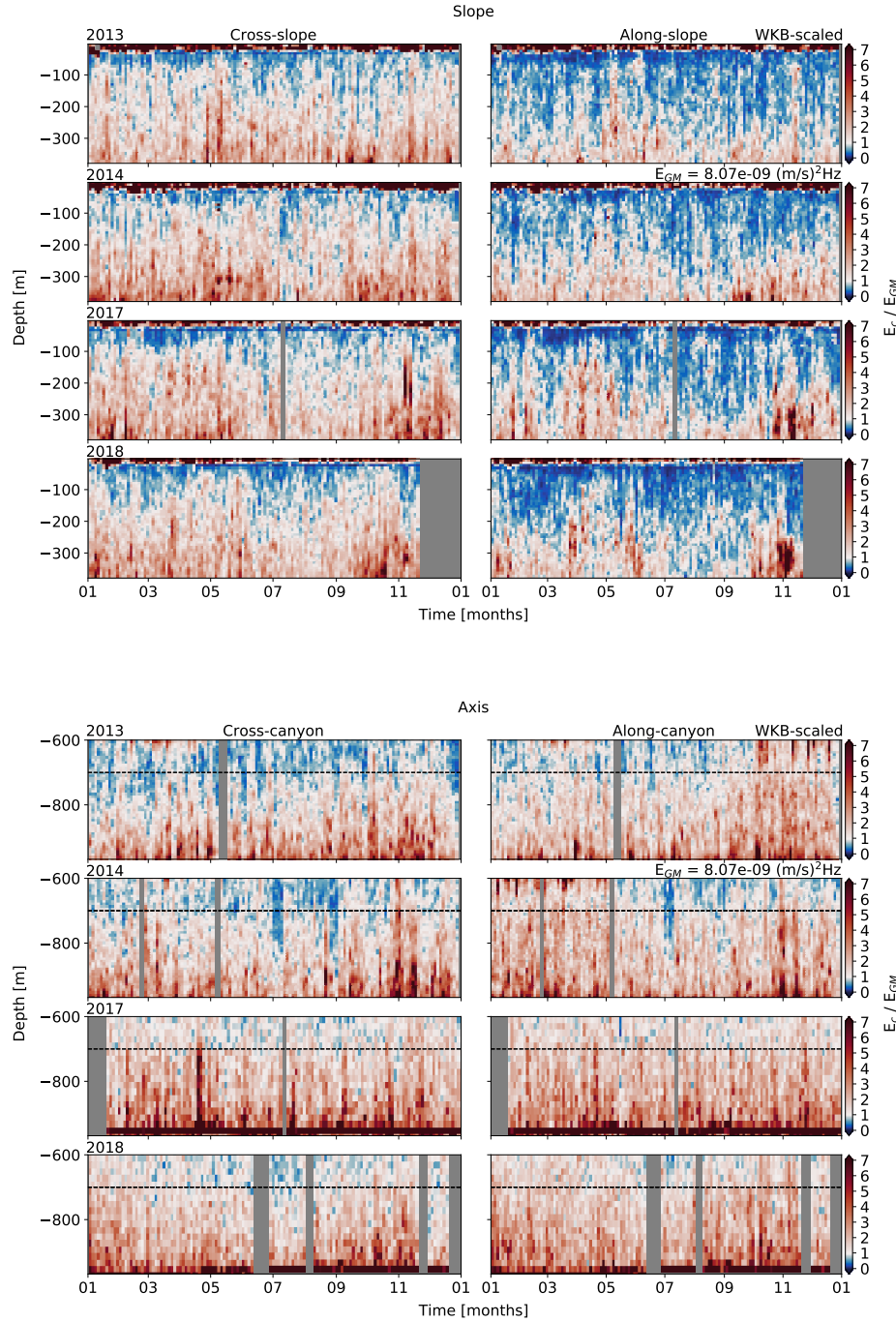


**Figure 32.** Continuum energy ( $E_c$ ) versus component-wise GM energy ( $E_{GM}$ ), for Slope (top) and Axis (bottom). Results are obtained from WKB-scaled spectra of horizontal velocity data. Continuum amplitudes are generally enhanced near topography, as compared to the open-ocean GM spectrum.

propagation, and VICS circulation and productivity (Crawford and Thomson, 1984; Cummins and Oey, 1997).

As the diurnal (and sub-diurnal) frequency is sub-inertial, diurnal IT are evanescent (trapped) to topography north of their turning latitude ( $\sim 30^\circ\text{N}$ ), unable to radiate offshore. This is consistent with the likely barotropic forcing observed, and Cummins and Oey (1997) found that trapped sub-inertial diurnal IT generation was prevalent on the VICS adjacent continental slope, similar to other Pacific slopes (Rudnick, 2015) and seamounts (Robertson et al., 2017). It is unlikely for there to be incident baroclinic diurnal IW or IT unless they propagate along the shelf. However, if a diurnal phase-lag of up to a day is present, as at Slope, this could suggest a baroclinic generation site within about 200 km, based on a  $K_1$  mode-1 wave speed of about 2 m/s (Crawford and Thomson, 1984). One candidate would be diurnal shelf waves generated by oscillatory tidal currents near the mouth of the Juan de Fuca Strait ( $\sim 100$  km east) that propagate poleward along the VICS (Crawford and Thomson, 1984; Flather, 1988). Confirmation of such waves would require additional instruments along the shelf, and is beyond the scope of this study. Other regions thought to be productive for baroclinic diurnal waves are either disconnected from the shelf (e.g. the abyssal Juan de Fuca Ridge) and cannot propagate sub-inertially to Barkley Canyon (Lavelle and Cannon, 2001), or too distant for the observed phase-lag (e.g. Mendocino Escarpment, 900 km south; Morozov, 2018). As there is enough uncertainty in the correlations that the phase-lag could effectively be null, and considering the vertically linear structure, it seems likely that the diurnal band is primarily forced by the local barotropic spring-neap cycle, with possible seasonal contributions from shelf-waves, mean current interactions, or stratification.

In contrast, the semidiurnal tides are super-inertial, able to freely propagate away from topography as IT. It is not unlikely that there could be incident remote semidiurnal IT at Barkley Canyon, contributing to the highly variable response. For a semidiurnal phase-lag up to four days, as at Slope, a regional mode-1  $M_2$  phase speed of  $c_1 \sim 3.0$  m/s (Zhao et al., 2016) suggests a baroclinic generation site up to 1000 km away. A likely origin is the Mendocino Escarpment running E-W off of Northern California, one of the strongest generation sites for low-mode semidiurnal IT in the northeast Pacific (Althaus et al., 2003; Arbic et al., 2012; Zhao, 2017; Morozov, 2018). Strong tide-topography generated northward propagating mode-1  $M_2$  IT, along with the escarpment's location about 800 km due south of Barkley Canyon ( $\sim 3.5$  days), agree reasonably within the observed phase lag. Other potential generation sites are closer (e.g. mouth of Juan de Fuca Strait  $\sim 100$  km, or Juan de

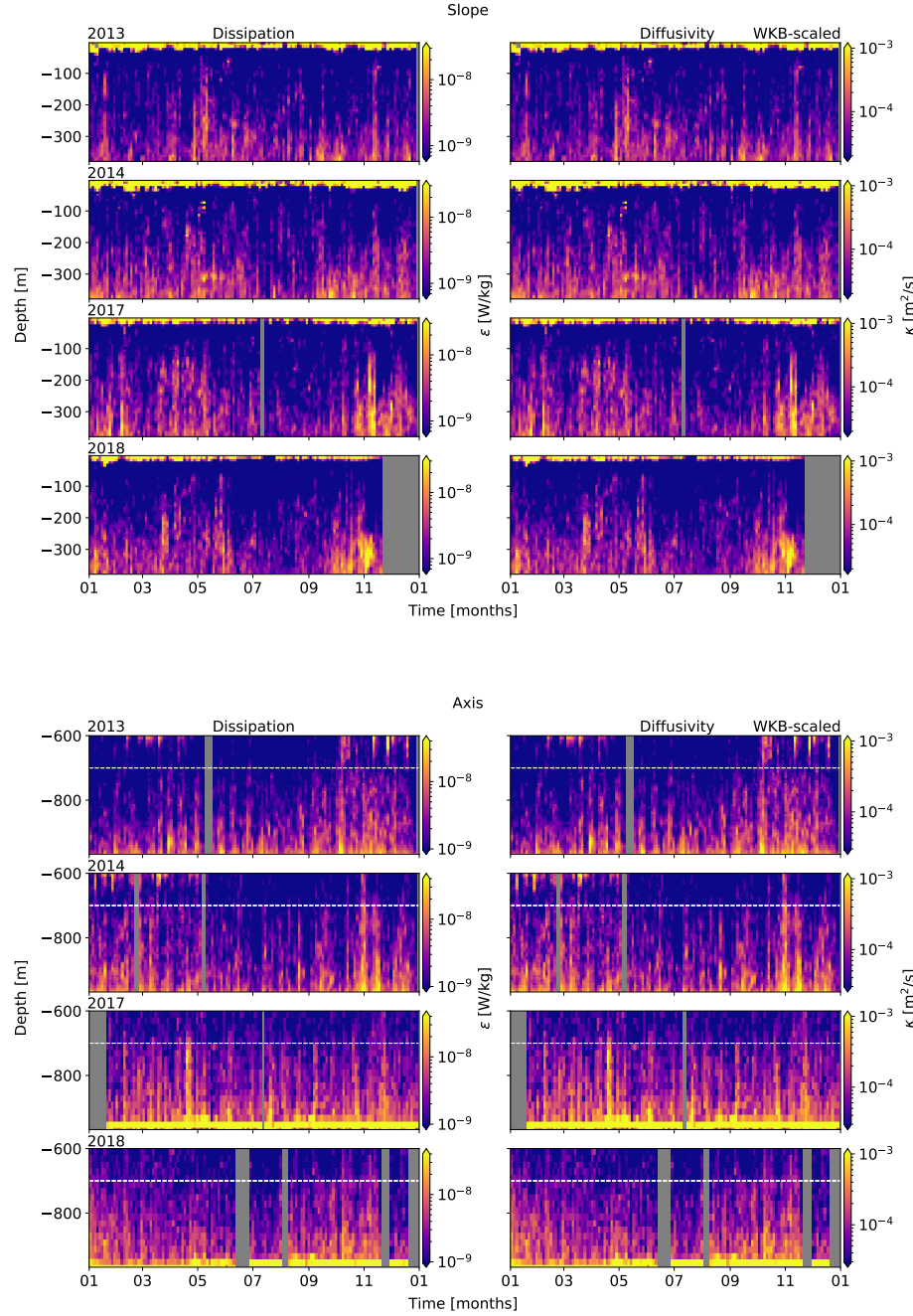


**Figure 33.** Dissipation rates (left) and turbulent eddy diffusivity (right), for WKB-scaled horizontal velocity spectra at Slope (top) and Axis (bottom). Both dissipation and diffusivity are heightened near topography.

Fuca Ridge  $\sim$ 400 km) or are somewhat obstructed by land (e.g. Haida Gwaii Islands), but could still contribute.

For free IW and IT, such as incident semidiurnal IT, the criticality of the impacted topography can lead to focusing and breaking, or reflection. Barkley Canyon is generally supercritical or near-critical to incident semidiurnal IT (Figure 4). Critical slope regions were determined from the gradient of bathymetry data obtained from the National Oceanic and Atmospheric Administration (NOAA) National Centre for Environmental Information, as 3 arc-second resolution mean sea level depth. At the Slope site, the local slope is  $\beta \approx 0.060$ , supercritical to the semidiurnal propagation angle  $\alpha_{M2} \approx 0.026$  at that depth (Figure 6). This suggests downward reflection (CW) and focusing of incident semidiurnal IT. The Slope site sits adjacent to a large near-critical region below the shelf-break (Figure 4), which, along with the VICS itself, is another source of observed downward semidiurnal energy (Drakopoulos and Marsden, 1993). For the Axis site on the canyon floor, the local slope angle is  $\beta \approx 0.019 < \alpha_{M2} \approx 0.036$  (Figure 6). As such, this portion of the canyon floor is subcritical to semidiurnal IT, suggesting upward reflection. However, as the canyon walls are generally supercritical, and the surrounding floor is near-critical (Figure 4), the propagation of semidiurnal IT at Axis is likely complex. Xu and Noble (2009) found that deep in Monterey Canyon semidiurnal IT were not only scattered up-canyon along the subcritical floor from the mouth, but also reflected down by the supercritical walls, highly focusing semidiurnal energy near the bottom. The potential for scattering, reflection, focusing, and generation of semidiurnal IT all at Axis could lead to highly 'channeled' deep-canyon semidiurnal response.

Together, the irregular nature of the semidiurnal phase-lag and the potential for critical IT-topography interactions suggests that forcing is a mix of local barotropic and remote incident IT. As the barotropic tide passes over Barkley Canyon, near-critical slope topography generates and focuses semidiurnal IT, which radiate downward from the shelf-break to the slope and canyon, where further downward reflection and focusing occurs. Remote incident IT are also subject to these effects, and alter observed spring-neap phase based on their site of origin, likely Mendocino Escarpment to the south. Finally, as little annual seasonality in the local barotropic spring-neap forcing cannot explain large-scale inter-annual features in the observations, such as the consistent spring pulse at Slope, secondary contributors may include seasonal changes to stratification and mean currents (Drakopoulos and Marsden, 1993; Cummins et al., 2000).

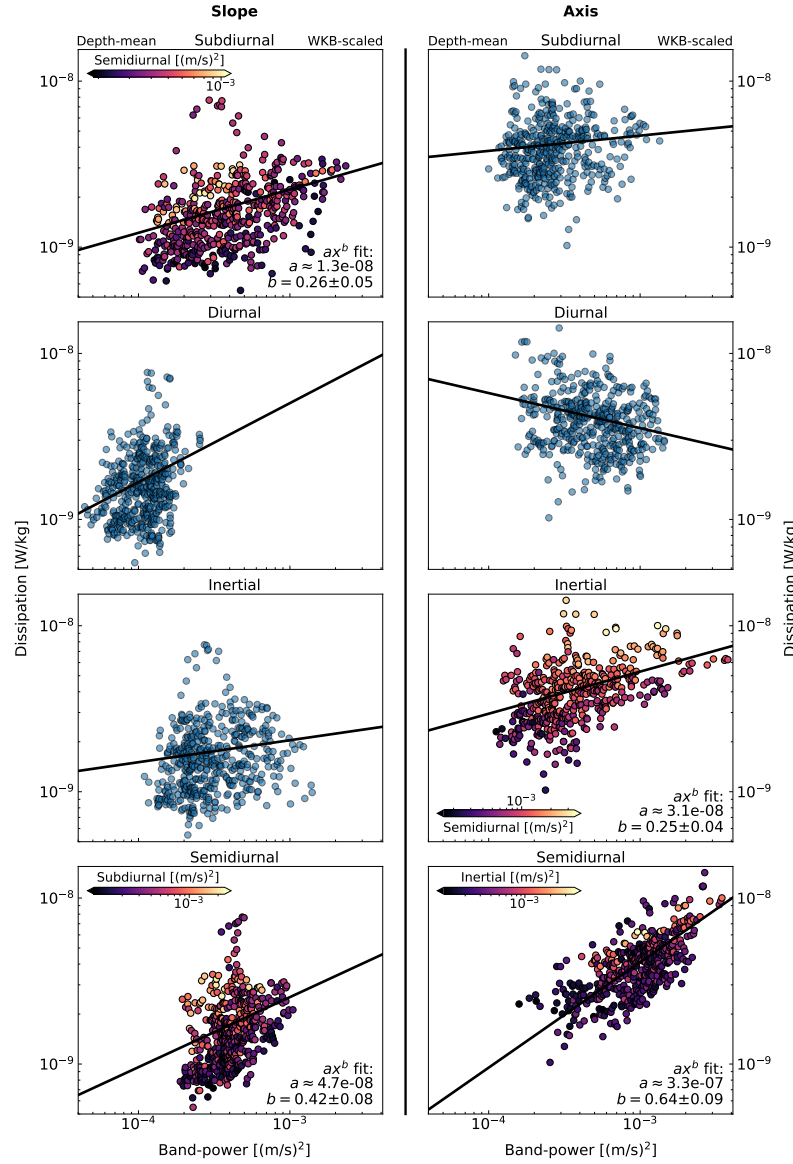


**Figure 34.** Dissipation power law fits. Scatter plots are for depth-mean WKB-scaled depth-band power at Slope (left) and Axis (right), all years. Frequency constituents are listed for each row, as sub-diurnal (top), diurnal (second), NI (third), and semidiurnal (bottom). Black lines indicate the power law fit, listed in the lower-right of each frame. For each site, the two most likely contributors are coloured by the strength of the other.

### 7.3 Near-inertial forcing

NI IW generated by wind events are thought to be significant contributors to mixing in the deep ocean, of similar magnitude to the conversion of barotropic tide to baroclinic internal tide energy (Alford et al., 2012). It is interesting that NI band-power can be so strongly attenuated with depth at Slope, while eliciting a deep response at Axis. The timing of these events is linked, so the difference in topography likely affects the response; however, this relationship is not well discussed in the literature. It may be that canyon topography responds differently to the modal structure of ML generated NI waves. Mode-1 amplitudes up to 0.6 m/s occur after notable wind events, similar to findings by Jarosz et al. (2007) in DeSoto Canyon, who found that while low modes generally dominate, more NI activity is observed when the ML is thin and high modes are prevalent. Alford et al. (2016) note that it is high mode waves that propagate downward, while low mode waves contribute more to horizontal propagation. Ultimately, the downward propagation of NI IW is difficult to characterise as there are many additional factors to consider, such as topography, seasonal thermocline thickness,  $\beta$ -plane effects, and near-surface mesoscale vorticity adjusting local  $f_0$  (Alford et al., 2016).

Regarding the delayed NI deep response to wind events, D'Asaro (1995) made a similar observation of an 8-10 day event, and determined that the divergence-forced NI pumping at the ML base causes oscillating pressure gradients in the thermocline, accelerating NI currents at depth. The rate of vertical energy transfer depends on the horizontal scale of the ML NI currents, with smaller horizontal scale ML currents propagating vertical energy faster. As vertical modes have progressively slower horizontal group velocities, the low modes propagate their energy away, first. As the low mode energy propagates away, the available energy and horizontal scale of the ML inertial currents decreases. Vertical energy propagation into the thermocline increases accordingly, with a notable maximum associated with a timescale of the departure of modes 1 and 2. Additionally, the beta effect also decreases the north-south horizontal wavenumber,  $l$ , with time, which in turn decreases the horizontal scale of the ML NI currents.

The results suggest that NI forcing is complex, dependent on variable characteristics of both wind events and ML processes, leading to highly intermittent seasonality in the interior. Remote forcing is also possible, as free NI IW generated at the base of the surface mixed-layer must propagate equatorward due to the effects of turning latitudes (Alford et al., 2016). There is often a blue-shift of the  $f$  spectral peak associated with remote NI forcing (Garratt, 1977; Voelker et al., 2020); however, high frequency-resolution spectra (Figure

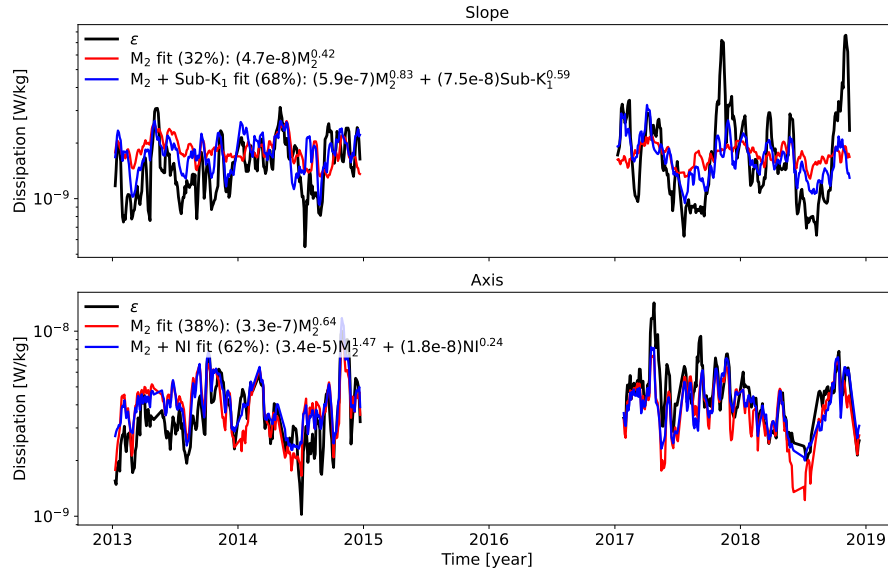


**Figure 35.** Dissipation multi-variate power law fits for Slope (top) and Axis (bottom). Comparison time series of depth-mean WKB-scaled dissipation (black), semidiurnal power law fits (red), and multi-variate power law fits (blue). Percent good is listed for each fit, as a measure of which fit line is closest to  $\epsilon$  at each time step.

39) do not resolve any additional NI peaks. Wind forcing correlations may be further complicated by the location of the weather buoy, 50 km north of Barkley Canyon. Regardless, strong qualitative and moderate quantitative correlations suggest that NI observations are most responsive to wind events when the ML is thin and high-mode contributions are prevalent, particularly in the late-summer and fall. Potential secondary forcing of deep NI response could be from mean currents or lee waves of NI frequency across the mouth or rim of the canyon, where topographic attenuation effects may be reduced due to the openness of these areas. Alford (2016) stated that “neither the decay of mixed-layer motions nor the rate of energy transfer into the deep ocean can adequately be predicted for the best-documented storm response on record”, summarising the effectiveness of attempting to characterise vertical NI processes. Needless to say, additional research is necessary, and beyond the scope of this study.

## 7.4 Dissipation forcing (incomplete)

## 7.5 Spectral shoulder (incomplete)

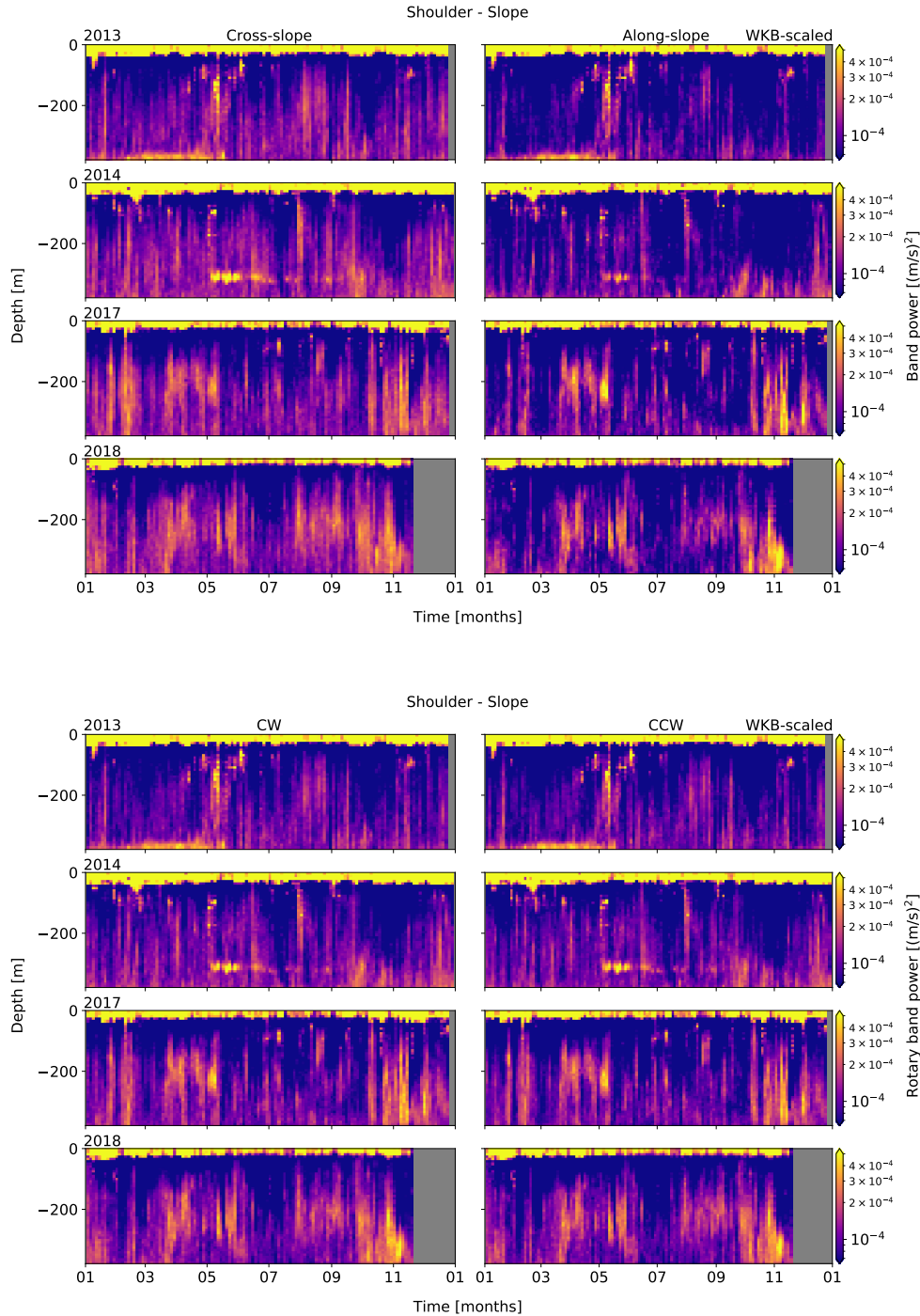


**Figure 36.** Band-integrated shoulder PSD (upper) and rotary (lower) spectra for Slope, from WKB-scaled horizontal velocity data. Cross- (left) and along-slope (right) components are shown. Each row represents an analysis year, labelled at upper-left.

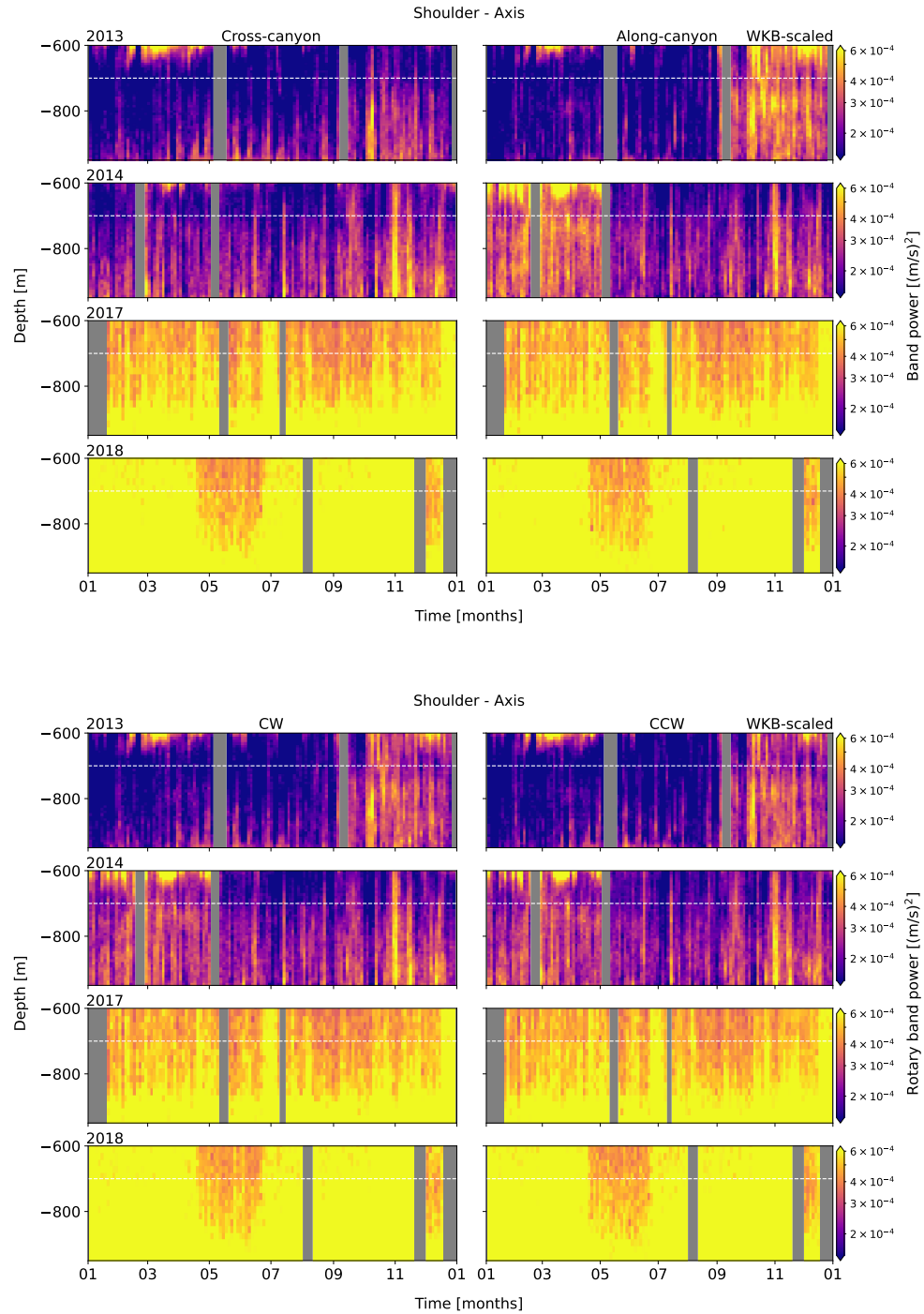


**Figure 37.** Band-integrated shoulder PSD (upper) and rotary (lower) spectra for Axis, from WKB-scaled horizontal velocity data. Cross- (left) and along-slope (right) components are shown. Each row represents an analysis year, labelled at upper-left. 2017 and 2018 are contaminated by the Nortek 55 kHz instrument noise floor.

## 8 Summary and conclusions

It was found that there is significant influence from topography on the local IW field at both sites, guiding flow (with consistent up-canyon currents above a thin down-canyon layer) and causing frequency-dependent focusing (or attenuation, for NI at Slope) of spectral power, generally up to  $2\times$  orders of magnitude 130 m AB at Slope, and up to  $3\times$  orders of magnitude 230 m AB at Axis. The near-topography enhancement has unique seasonality for individual frequency constituents that varies little inter-annually. Sub-diurnal and diurnal flows are sub-inertially trapped along topography, and the diurnal band appears to be forced locally (barotropically). Free semidiurnal IT are focused and reflected near critical topography, and appear to experience both local and remote (baroclinic) forcing. The NI band is attenuated near the slope, yet enhanced near the canyon bottom, with intermittent forcing that appears linked to regional wind events, high-mode propagation, and the seasonal ML depth. The state of the IW continuum is elevated as compared to the open-ocean GM spectrum (up to  $7\times$  GM), with enhanced dissipation (exceeding  $10^{-8}$  W/kg) and diffusivity (exceeding  $10^{-4}$  m<sup>2</sup>/s) near topography. Power-dissipation seasonality correlations suggest a cascade of energy from the semidiurnal constituent, yielding inter-annual power law relationships of  $\epsilon \sim M_2^{0.42}$  at the slope, and  $\epsilon \sim M_2^{0.64}$  in the canyon. Improved fits accounting for secondary constituents (Sub<sub>K1</sub> on the slope, and NI in the canyon yield) yield power law relationships of  $\epsilon \sim M_2^{0.83} + \text{Sub}_{K1}^{0.59}$  at the slope, and  $\epsilon \sim M_2^{1.47} + \text{NI}^{0.24}$  in the canyon. There is also evidence of a spectral shoulder near  $N$  which shares power seasonality with the internal wave continuum, yielding a power law relationship of  $P_{sh} \sim \epsilon^{0.36}$  at the slope, and  $P_{sh} \sim \epsilon^{0.48}$  in the canyon.

Unfortunately, the WKB-stretch scaling applied throughout much of the analysis is based on deep CTD casts that were made nearby (20 km S), but away from topography; the stratification profile captures the surface ML and pycnocline, but does not account for stratification adjustment near the slope or in the canyon (Figure 8). Hotchkiss and Wunsch (1982) noted increased stratification near areas of high 'topographic relief', such as the shelf-break and slopes. These highly stratified turbulent layers experience the effects of reflection, scattering, and IT and lee-wave generation, as well as amplification of IW and IT. To properly mitigate the effects of depth dependent stratification variability, further research would benefit from site specific climatology data.

Results could also be improved through increased sampling consistency between instruments (there were maintenance periods and instrument redeployments during analysis years), additional instrument sites (along the canyon

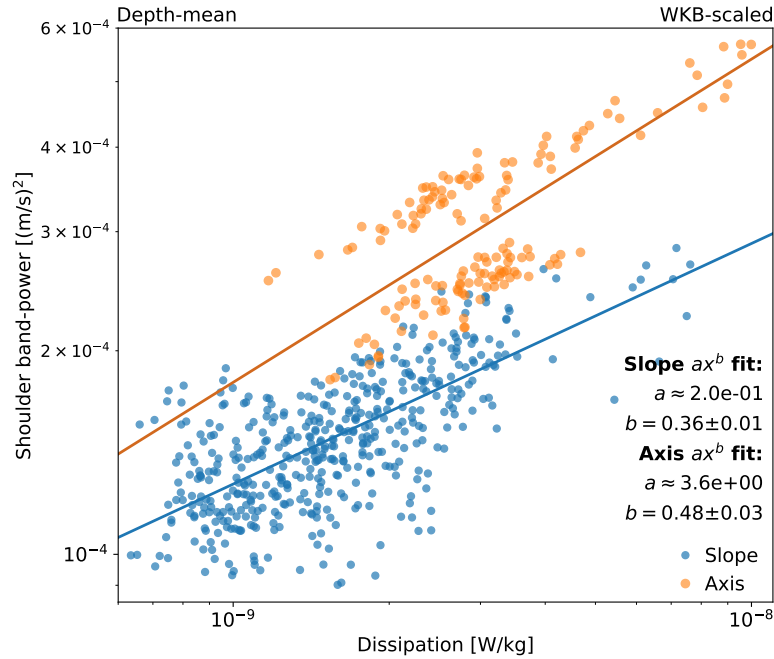


**Figure 38.** Power law relationship between dissipation and the spectral shoulder. Inter-annual depth-mean scatter plot for WKB-scaled dissipation and shoulder depth-band power, for Slope (blue) and Axis (orange).

floor and rim), and additional overlapping comparison years between sites. Broader temporal coverage could provide insight into decadal seasonality, while additional spatial coverage would allow for observations of IW propagation. For NI wind forcing, reanalysis wind data may have provided better (fewer gaps) temporal coverage for comparison. Furthermore, this study was not able to identify forcing for the periodicity of the shoaling up-canyon mean currents at Axis, the sub-diurnal range's intermittent seasonality, or accurately identify sites of origin for incident baroclinic IT.

Barkley Canyon is a dynamic submarine canyon and slope region with physical processes that are heavily influenced by topography. Currents, tides, and wind all contribute to an energetic region of IW and IT, driving mixing and other dissipative processes. As canyons and slopes are known as hot-spots for IW driven mixing, contributing significantly to regional transport of energy, shelf productivity, and even large-scale ocean circulation and climate effects, ONC's NEPTUNE cabled observatory is an important network for further investigation of the VICS, and beyond. Due to the accessibility of publicly available

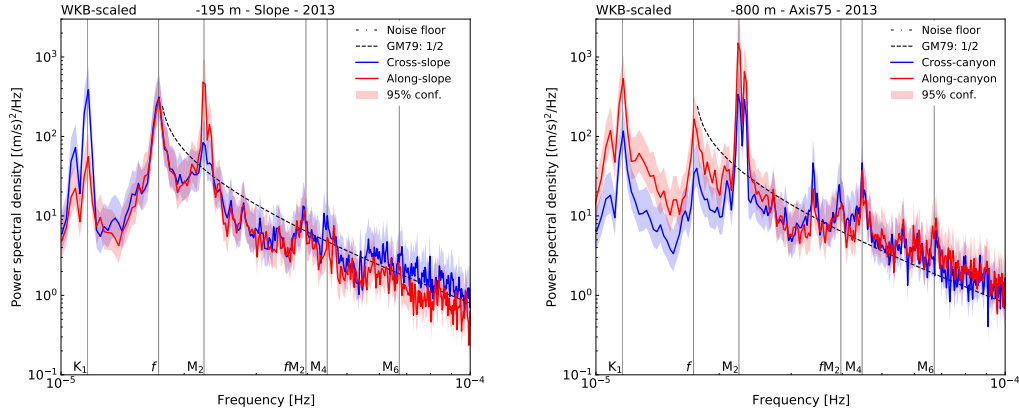


**Figure 39.** High frequency-resolution mid-depth PSD of WKB-scaled horizontal velocity data, for Slope (left) and Axis (right), in 2013. Frequency scale is zoomed to the tidal range. There are no additional peaks or apparent blue-shift for the NI constituent, suggesting local forcing.

data, Barkley Canyon is a key observational laboratory for not only furthering ocean research, but fostering collaboration between members of the amateur and professional scientific communities. It is hoped that this study has provided insight leading to such research and collaboration, as well as a better understanding of the importance of shelf-incising canyons as fundamental to physical ocean processes.

### 8.1 ETC - does this writing belong anywhere?

*Intensified near-slope layers are not uncommon, and are usually driven by focused incident IW energy that enhances up-slope flow (Polzin et al., 1997; Nash et al., 2004; Kunze et al., 2012). Hotchkiss and Wunsch (1982) found a  $\sim 10\times$  increase in near-slope IW energy near Hudson Canyon, with a depth-dependent vertical scale of about 150 m AB at -400 m depth.*

*Drakopoulos and Marsden (1993) associated strengthened diurnal tidal flow over the VICS with increased stratification in summer, while Cummins et al. (2000) suggest that diurnal tidal currents over the VICS are seasonally responsive to the large-scale spring shift to equatorward upwelling-favourable mean currents, a consistent inter-annual process in the region. Similar results were noted by Xu and Noble (2009), who found inter-annually consistent  $K_1$  currents in Monterey Canyon that peaked relative to the annual cycle of spring/neap-tide forcing.*

*Thomson et al. (1990) found that NI IW become increasingly attenuated as*

*they approach slopes, absorbed by strong vertical shear in the background flow associated with topographically trapped oscillations. Intermittent forcing of NI IW is common; small ( $\sim 100$  km) southward cold fronts and lows with considerable CW NI rotation are the most significant sources of NI flux, more-so than even synoptic scale systems, and occur most often in fall and early-winter (D'Asaro, 1985; Alford, 2001; Voelker, 2020). Additionally, seasonally variable pycnocline and mixed-layer (ML) depths have been observed to modulate NI energy by up 12 $\times$  when thin, by affecting stratification-dependent modes 'strummed' by ML NI currents which generate NI IW through divergent 'pumping' at the ML base (Jarosz et al., 2007). The variability of wind events and near-surface conditions all contribute to highly intermittent forcing that is both difficult to model and correlate, and is not possible to address with single mooring data (Alford et al., 2012).*

*This initial propagation period has been associated with the separation of the first few modes (Gill, 1984; D'Asaro, 1995), described as 'inertial beating', where the horizontal departure of each mode increases vertical propagation of NI energy (Zervakis and Levine, 1995). Time-scales for the departure of mode-1 and mode-2 are associated with a transfer of NI energy from the ML to the upper-pycnocline, up to 10-20 days, after which the deep response rapidly increases and NI energy is evenly distributed between the pycnocline and lower depths (Zervakis and Levine, 1995). This quick radiation of NI energy to deep water is associated with 'inertial jets' of CW relative vorticity originating near the upper pycnocline, possibly induced by mesoscale fronts (Kunze, 1985; D'Asaro, 1995; Zhai et al., 2005; Alford et al., 2016).*

*This is not surprising, as it has been shown that where criticality ( $\beta/\alpha$ , as detailed in section 3) is near to 1, typically below the shelf-break, incident semidiurnal IT are most strongly subject to near-slope focusing and reflection (Robertson et al., 2017). At other slope sites, there is evidence of elevated near-bottom energy-flux associated with both semidiurnal IT generation and incident reflection, with topographically dependent vertical scales within a few hundred metres AB (Terker et al., 2014; Xie and Chen, 2021). Locally, Drakopoulos and Marsden (1993) found that seaward of the VICS shelf break that semidiurnal IT propagation was strongly CW downward - noted at other slope sites (Subeesh et al., 2021) - and attributed to incident IT downward reflection and seaward generation from the shelf and near-critical shelf-break.*

*Drakopoulos and Marsden (1993) found that the semidiurnal IT on the VICS continental margin gained strength in the late-spring through summer, attenuating by September, associated with seasonal changes in stratification.*

*IW energy is known to cascade from low- (tidal and sub-tidal) to high-frequency (continuum) processes, with continuum seasonality reflecting such a transfer of energy (Polzin, 2004). Topographic focusing of low-frequency IW enhances the cascade of energy to high-frequency dissipative processes, elevating the continuum amplitude and driving mixing (Polzin, 2004). At Slope, the most powerful frequency constituents are the sub-diurnal currents and semidiurnal IT. At Axis, sub-diurnal currents are weakened and the focused semidiurnal IT dominate throughout the year, though the occasional NI pulse makes it into the canyon in fall (e.g. see November 2014, Figures 24 and 30). These bands contribute the most energy to dissipation, driving observed continuum seasonality. However, there are likely additional contributions from other bands, and unknown effects due to physical processes beyond the scope of this study.*

## 9 Appendix A: Supplemental plots

### 9.1 Wind comparisons

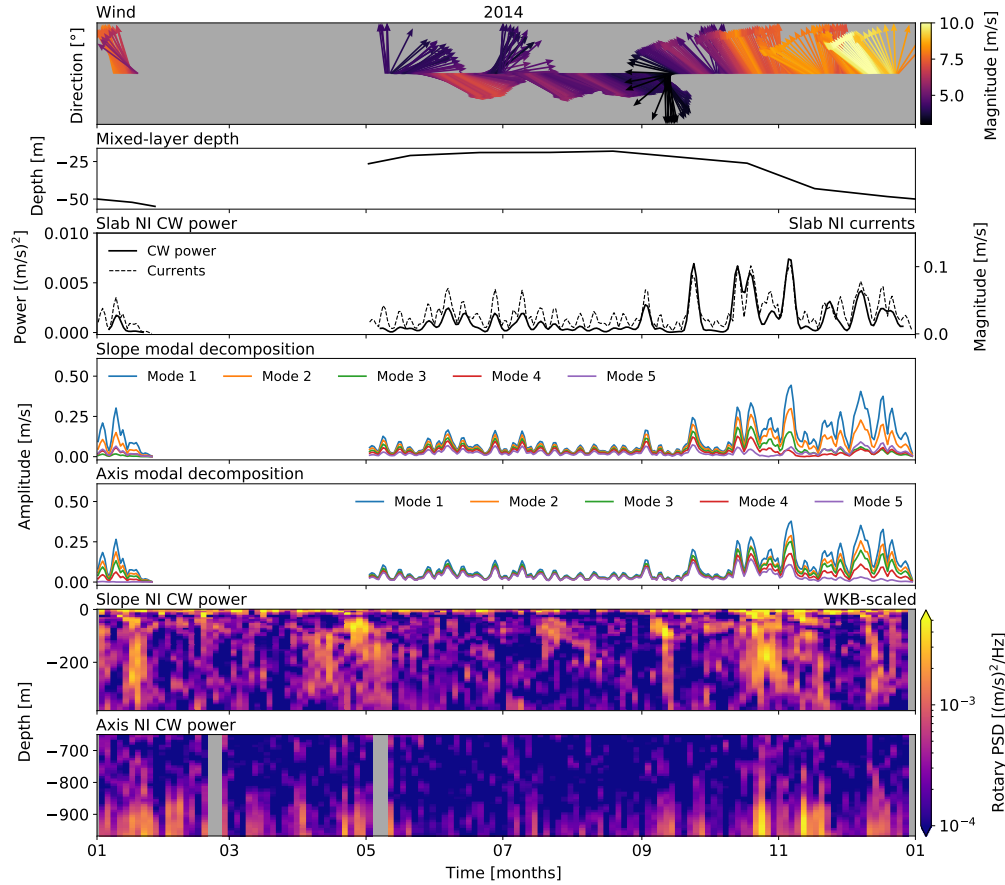


**Figure 40.** NI forcing analysis for 2014. Panels are (i) wind direction and amplitude, (ii) monthly-averaged ML depth for Line P station 3 as determined by Li et al. (2005), (iii) slab model NI CW power and NI currents, (iv, v) seasonal mode amplitudes for Slope and Axis, and (vi, vii) band-integrated NI CW power at Slope and Axis. There appears to be a complex relationship between the wind, ML, slab currents, and mode amplitudes in driving the NI observations, with the most obvious effects in the fall.

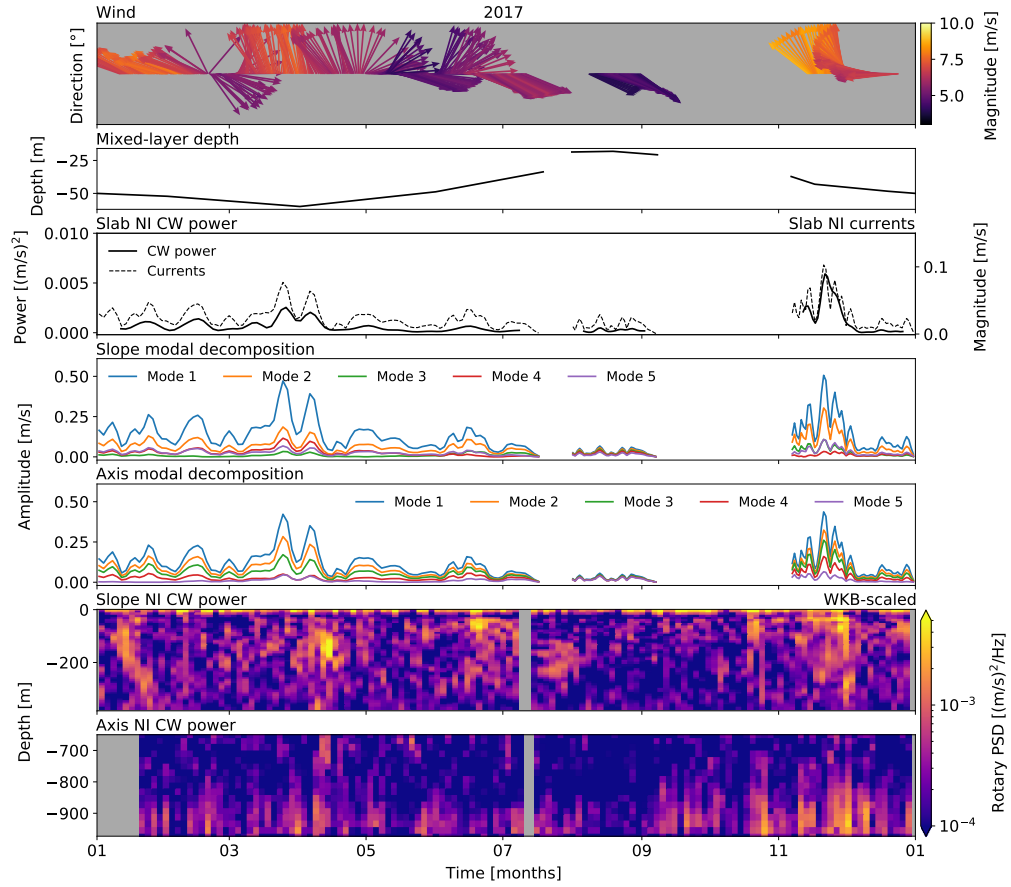


**Figure 41.** NI forcing analysis for 2017. Panels are (i) wind direction and amplitude, (ii) monthly-averaged ML depth for Line P station 3 as determined by Li et al. (2005), (iii) slab model NI CW power and NI currents, (iv, v) seasonal mode amplitudes for Slope and Axis, and (vi, vii) band-integrated NI CW power at Slope and Axis. There appears to be a complex relationship between the wind, ML, slab currents, and mode amplitudes in driving the NI observations, with the most obvious effects in the fall.

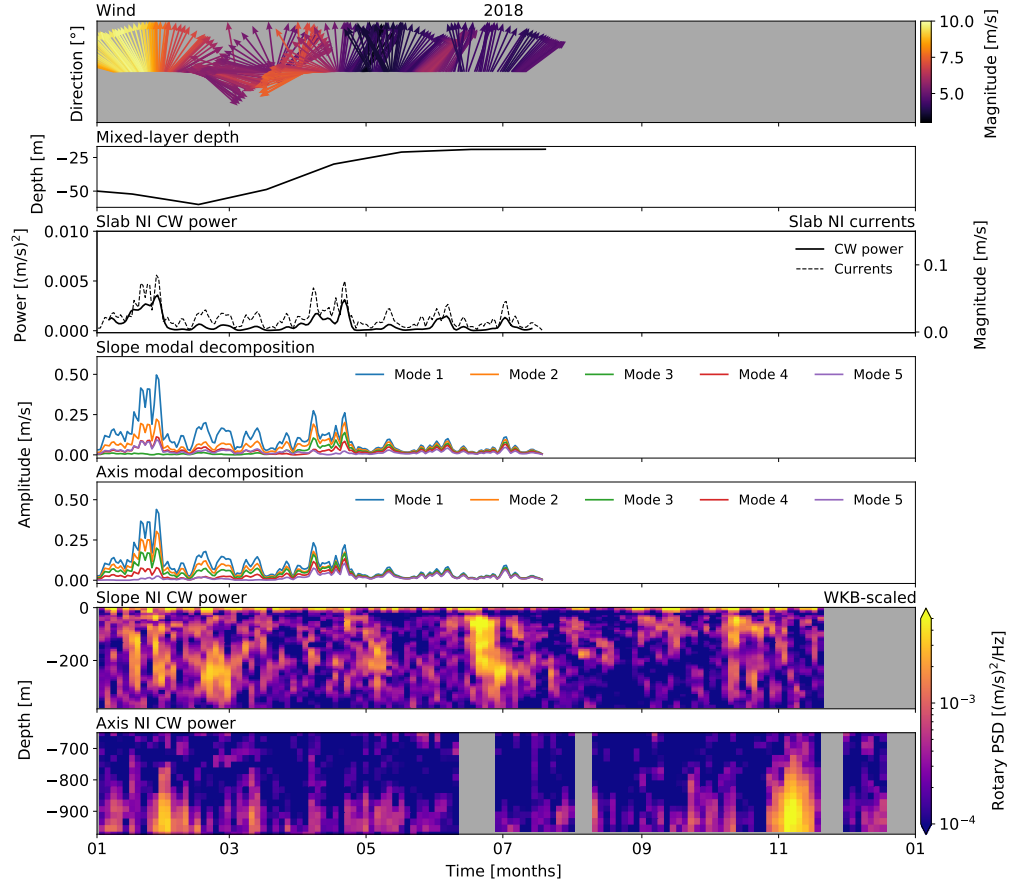


**Figure 42.** NI forcing analysis for 2018. Panels are (i) wind direction and amplitude, (ii) monthly-averaged ML depth for Line P station 3 as determined by Li et al. (2005), (iii) slab model NI CW power and NI currents, (iv, v) seasonal mode amplitudes for Slope and Axis, and (vi, vii) band-integrated NI CW power at Slope and Axis. There appears to be a complex relationship between the wind, ML, slab currents, and mode amplitudes in driving the NI observations, with the most obvious effects in the fall.

## 10 References (incomplete)

*Incomplete*

- Alford, M. H., MacKinnon, J. A., Zhao, Z., Pinkel, R., Klymak, J., & Peacock, T. (2007). Internal waves across the Pacific. *Geophysical Research Letters*, 34(24), 24601. <https://doi.org/10.1029/2007GL031566>
- Alford, M. H., Cronin, M. F., & Klymak, J. M. (2012). Annual cycle and depth penetration of wind-generated near-inertial internal waves at ocean station papa in the northeast pacific. *Journal of Physical Oceanography*, 42(6), 889–909. <https://doi.org/10.1175/JPO-D-11-092.1>
- Allen, S. E., Vindeirinho, C., Thomson, R. E., Foreman, M. G. G., & Mackas, D. L. (2001). Physical and biological processes over a submarine canyon during an upwelling event. *Canadian Journal of Fisheries and Aquatic Sciences*, 58(4), 671–684. <https://doi.org/10.1139/f01-008>
- Anstey, K. (2022). Internal Waves at Barkley Canyon. *Github repository*. Accessed from [https://www.github.com/kurtisanstey/internal\\_waves\\_barkley\\_canyon/](https://www.github.com/kurtisanstey/internal_waves_barkley_canyon/)
- Carter, G. S., & Gregg, M. C. (2002). Intense, variable mixing near the head of Monterey Submarine Canyon. In *Journal of Physical Oceanography* (Vol. 32). [https://doi.org/10.1175/1520-0485\(2002\)032j3145:IVMNTH;2.0.CO;2](https://doi.org/10.1175/1520-0485(2002)032j3145:IVMNTH;2.0.CO;2)
- Crawford, W. R., & Thomson, R. E. (1984). Diurnal-Period Continental Shelf Waves along Vancouver Island: A Comparison of Observations with Theoretical Models. *Journal of Physical Oceanography*, 14(10), 1629–1646. [https://doi.org/10.1175/1520-0485\(1984\)014j1629:dpcswa;2.0.co;2](https://doi.org/10.1175/1520-0485(1984)014j1629:dpcswa;2.0.co;2)
- Cummins, P. F., Masson, D., & Foreman, M. G. G. (2000). Stratification and mean flow effects on diurnal tidal currents off Vancouver Island. *Journal of Physical Oceanography*, 30(1), 15–30. [https://doi.org/10.1175/1520-0485\(2000\)030j0015:SAMFEO;2.0.CO;2](https://doi.org/10.1175/1520-0485(2000)030j0015:SAMFEO;2.0.CO;2)
- D'Asaro, E. A. (1985). The energy flux from the wind to near-inertial motions in the surface mixed layer. *J. Phys. Oceanogr.*, 15(8, Aug. 1985), 1043–1059. [https://doi.org/10.1175/1520-0485\(1985\)015j1043:tefftw;2.0.co;2](https://doi.org/10.1175/1520-0485(1985)015j1043:tefftw;2.0.co;2)
- Drakopoulos, P. G., & Marsden, R. F. (1993). The internal tide off the west coast of Vancouver Island. *Journal of Physical Oceanography*, 23(4), 758–775. [https://doi.org/10.1175/1520-0485\(1993\)023j0758:TITOTW;2](https://doi.org/10.1175/1520-0485(1993)023j0758:TITOTW;2)

.0.CO;2

- Garratt, J. R. (1977). Review of Drag Coefficients over Oceans and Continents. [https://doi.org/10.1175/1520-0493\(1977\)1052.0.CO;2](https://doi.org/10.1175/1520-0493(1977)1052.0.CO;2)
- Garrett, C., & Munk, W. (1979). internal waves in the Ocean. In Ann. Rev. Fluid Mech (Vol. 11).
- Gemmrich, J., & Klymak, J. M. (2015). Dissipation of internal wave energy generated on a critical slope. *Journal of Physical Oceanography*, 45(9), 2221–2238. <https://doi.org/10.1175/JPO-D-14-0236.1>
- Gonella, J. (1972). A rotary-component method for analysing meteorological and oceanographic vector time series (Vol. 19). Pergamon Press.
- Hendershott, M. C., & Garrett, C. (2018). Internal Tides. In Geophysical Fluid Dynamics (No. 6). Retrieved from <https://gfd.whoi.edu/wp-content/uploads/sites/18/2018/03/lecture0621>
- Hotchkiss, F. S., & Wunsch, C. (1982). Internal waves in Hudson Canyon with possible geological implications. *Deep Sea Research Part A, Oceanographic Research Papers*, 29(4), 415–442. [https://doi.org/10.1016/0198-0149\(82\)90068-1](https://doi.org/10.1016/0198-0149(82)90068-1)
- Johnston, T. M. S., & Rudnick, D. L. (2015). Trapped diurnal internal tides, propagating semidiurnal internal tides, and mixing estimates in the California Current System from sustained glider observations, 2006–2012. *Deep-Sea Research Part II: Topical Studies in Oceanography*, 112, 61–78. <https://doi.org/10.1016/j.dsr2.2014.03.009>
- Klymak, J. M., Alford, M. H., Pinkel, R., Lien, R. C., Yang, Y. J., & Tang, T. Y. (2011). The breaking and scattering of the internal tide on a continental slope. *Journal of Physical Oceanography*, 41(5), 926–945. <https://doi.org/10.1175/2010JPO4500.1>
- Kundu, P. K., & Cohen, I. (2008). Fluid mechanics. (4th ed.). Academic Press.
- Kunze, E. (2017). Internal-wave-driven mixing: Global geography and budgets. *Journal of Physical Oceanography*, 47(6), 1325–1345. <https://doi.org/10.1175/JPO-D-16-0141.1>
- Kunze, E., Rosenfeld, L. K., Carter, G. S., & Gregg, M. C. (2002). Internal waves in Monterey Submarine Canyon. *Journal of Physical Oceanography*, 32(6), 1890–1913. [https://doi.org/10.1175/1520-0485\(2002\)032|1890:internal waveIMSCj2.0.CO;2](https://doi.org/10.1175/1520-0485(2002)032|1890:internal waveIMSCj2.0.CO;2)

- Kunze, E., Mackay, C., Mcphee-Shaw, E. E., Morrice, K., Girton, J. B., & Terker, S. R. (2012). Turbulent mixing and exchange with interior waters on sloping boundaries. *Journal of Physical Oceanography*, 42(6), 910–927. <https://doi.org/10.1175/JPO-D-11-075.1>
- Kuroda, H., Kusaka, A., Isoda, Y., Honda, S., Ito, S., & OniTuka, T. (2018). Diurnal tidal currents attributed to free baroclinic coastal-trapped waves on the Pacific shelf off the southeastern coast of Hokkaido, Japan. *Continental Shelf Research*, 158, 45–56. <https://doi.org/10.1016/j.csr.2018.02.010>
- Lamb, K. G. (2014). Internal wave breaking and dissipation mechanisms on the continental slope/shelf. *Annual Review of Fluid Mechanics*, 46, 231–254. <https://doi.org/10.1146/annurev-fluid-011212-140701>
- Levine, M. D. (2002). A modification of the Garrett-Munk internal wave spectrum. *Journal of Physical Oceanography*, 32(11), 3166–3181. [https://doi.org/10.1175/1520-0485\(2002\)032;3166:AMOTGM;2.0.CO;2](https://doi.org/10.1175/1520-0485(2002)032;3166:AMOTGM;2.0.CO;2)
- Li, M., Myers, P. G., & Freeland, H. (2005). An examination of historical mixed layer depths along Line P in the Gulf of Alaska. *Geophysical Research Letters*, 32(5), 1–4. <https://doi.org/10.1029/2004GL021911>
- Marques, O. B., Alford, M. H., Pinkel, R., MacKinnon, J. A., Klymak, J. M., Nash, J. D., ... Braznikov, D. (2020). Internal Tide Structure and Temporal Variability on the Reflective Continental Slope of South-eastern Tasmania. *Journal of Physical Oceanography*, 51(2), 611–631. <https://doi.org/10.1175/jpo-d-20-0044.1>
- Martini, K. I., Alford, M. H., Kunze, E., Kelly, S. M., & Nash, J. D. (2013). Internal bores and breaking internal tides on the Oregon continental slope. *Journal of Physical Oceanography*, 43(1), 120–139. <https://doi.org/10.1175/JPO-D-12-030.1>
- Mihaly, S. F., Thomson, R. E., & Rabinovich, A. B. (1998). Evidence for non-linear interaction between internal waves of inertial and semidiurnal frequency. *Geophysical Research Letters*, 25(8), 1205–1208. <https://doi.org/10.1029/98GL00722>
- Munk, W., & Garrett, C. (1979). Internal Waves and Small-Scale Processes. In C. Wunsch (Ed.), *Evolution of Physical Oceanography*.
- Nash, J. D., Kunze, E., Toole, J. M., & Schmitt, R. W. (2004). Internal tide reflection and turbulent mixing on the continental slope. In *Jour-*

- nal of Physical Oceanography (Vol. 34). [https://doi.org/10.1175/1520-0485\(2004\)034j1117:ITRATM;2.0.CO;2](https://doi.org/10.1175/1520-0485(2004)034j1117:ITRATM;2.0.CO;2)
- Polzin, K. L., & Lvov, Y. V. (2011). Toward regional characterizations of the oceanic internal wavefield. *Reviews of Geophysics*, 49(4), 4003. <https://doi.org/10.1029/2010RG000329>
- Robertson, R., Dong, J., & Hartlipp, P. (2017). Diurnal Critical Latitude and the Latitude Dependence of Internal Tides, Internal Waves, and Mixing Based on Barcoo Seamount. *Journal of Geophysical Research: Oceans*, 122(10), 7838–7866. <https://doi.org/10.1002/2016JC012591>
- Subeesh, M. P., Unnikrishnan, A. S., & Francis, P. A. (2021). Generation, propagation and dissipation of internal tides on the continental shelf and slope off the west coast of India. *Continental Shelf Research*, 214. <https://doi.org/10.1016/j.csr.2020.104321>
- Terker, S. R., Girton, J. B., Kunze, E., Klymak, J. M., & Pinkel, R. (2014). Observations of the internal tide on the California continental margin near Monterey Bay. *Continental Shelf Research*, 82, 60–71. <https://doi.org/10.1016/j.csr.2014.01.017>
- Thomson, R. E., & Crawford, W. R. (1982). The Generation of Diurnal Period Shelf Waves by Tidal Currents in: *Journal of Physical Oceanography* Volume 12 Issue 7 (1982). *Journal of Physical Oceanography*, 12(7).
- Thomson, R. E., Roth, S. E., & Dymond, J. (1990). Near-inertial motions over a mid-ocean ridge: Effects of topography and hydrothermal plumes. *Journal of Geophysical Research*, 95(C5), 7261. <https://doi.org/10.1029/jc095ic05p07261>
- Thomson, R. E., & Fine, I. V. (2003). Estimating mixed layer depth from oceanic profile data. *Journal of Atmospheric and Oceanic Technology*, 20(2), 319–329. [https://doi.org/10.1175/1520-0426\(2003\)020j0319:EMLDFO;2.0.CO;2](https://doi.org/10.1175/1520-0426(2003)020j0319:EMLDFO;2.0.CO;2)
- Thomson, R. E., & Emery, W. J. (2014). Data Analysis Methods in Physical Oceanography: Third Edition. In *Data Analysis Methods in Physical Oceanography: Third Edition (Third)*. <https://doi.org/10.1016/C2010-0-66362-0>
- Thomson, R. E., & Krassovski, M. V. (2015). Remote alongshore winds drive variability of the California Undercurrent off the British Columbia-Washington coast. *Journal of Geophysical Research: Oceans*, 120(12), 8151–8176. <https://doi.org/10.1002/2015JC011306>

- Voelker, G. S., Olbers, D., Walter, M., Mertens, C., & Myers, P. G. (2020). Estimates of wind power and radiative near-inertial internal wave flux: The hybrid slab model and IT application to the North Atlantic. *Ocean Dynamics*, 70(11), 1357–1376. <https://doi.org/10.1007/s10236-020-01388-y>
- Xie, X., & Chen, D. (2021). Near-surface reflection and nonlinear effects of low-mode internal tides on a continental slope. *Journal of Physical Oceanography*, 51(4), 1037–1051. <https://doi.org/10.1175/JPO-D-20-0197.1>
- Xie, X., Liu, Q., Zhao, Z., Shang, X., Cai, S., Wang, D., & Chen, D. (2018). Deep Sea Currents Driven by Breaking Internal Tides on the Continental Slope. *Geophysical Research Letters*, 45(12), 6160–6166. <https://doi.org/10.1029/2018GL078372>
- Zheng, J., Tian, J., & Liang, H. (2017). Observation of near-inertial internal waves on the continental slope in the northwestern South China Sea. *Journal of Ocean University of China*, 16(2), 184–190. <https://doi.org/10.1007/s11802-017-3153-7>